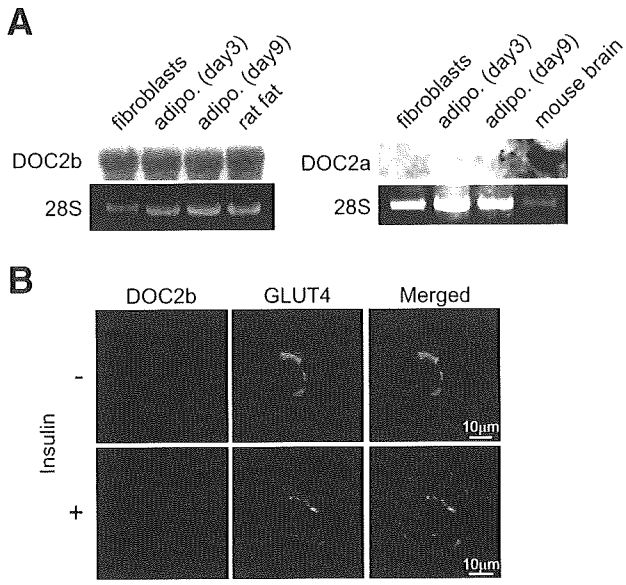

FIG. 1. The expression profiles and intracellular localization of DOC2b in 3T3-L1 adipocytes. *A*: The expressions of DOC2a and DOC2b in 3T3-L1 fibroblasts, 3T3-L1 adipocytes (days 3 and 9 of differentiation), rat epididymal fat, and mouse brain were analyzed by mRNA blot. *B*: Differentiated 3T3-L1 adipocytes were serum-starved for 3–4 h and then stimulated with 100 nmol/l of insulin for 20 min, fixed, and immunostained. The endogenous DOC2b and GLUT4 were visualized using anti-DOC2b and anti-GLUT4 antibodies and observed by confocal microscopy. (Please see http://dx.doi.org/10.2337/db08-0303 for a high-quality digital representation of this figure.)

RESULTS

DOC2b translocates to the plasma membrane in response to insulin. Type C tandem C2 domain proteins are classified into three groups (i.e., synaptotagmin and synaptotagmin-like protein and DOC2 family proteins). The first two groups of proteins regulate relatively fast membrane fusion (on the order of milliseconds to a few seconds) (12,13). This time scale is not suitable for GLUT4 vesicle fusion. Therefore, we focused on DOC2 family proteins as candidate regulators of GLUT4 vesicle fusion. First, we determined the expression profile of DOC2 mRNA in adipocytes. As shown in Fig. 1*A*, DOC2a was not expressed in 3T3-L1 adipocytes. According to a previous study, DOC2γ is localized to the nucleus and has no Ca^{2+}-binding activity because of amino acid substitutions at the Ca^{2+}-binding sites (14). Thus, we investigated the function of the DOC2b isoform involved in GLUT4 membrane fusion. Next, we examined the intracellular localization of DOC2b in differentiated 3T3-L1 adipocytes using anti-DOC2b antibody (Fig. 1*B*) or by expressing an eGFP fused to DOC2b (Fig. 2*A*). As shown in Fig. 1*B*, DOC2b results in a fine punctate or granular appearance throughout the cytoplasm under basal conditions. In contrast, the addition of insulin yields relatively slow (~5 min) translocation of DOC2b to the cell periphery (Fig. 2*A*). This time scale of translocation was very similar to that of GLUT4 vesicles. It is noteworthy that deletion of the MID enhanced plasma membrane localization even in the absence of insulin and that the C2B domain is necessary for membrane targeting (Fig. 2*B*). These observations are interesting in considering the distinct roles of the C2A and C2B domains and the negative regulatory function of MID. We performed additional experiments to determine the role of calcium in the translocation of DOC2b. As shown in Fig. 2*C*, the cell membrane permeable Ca^{2+}-chelating

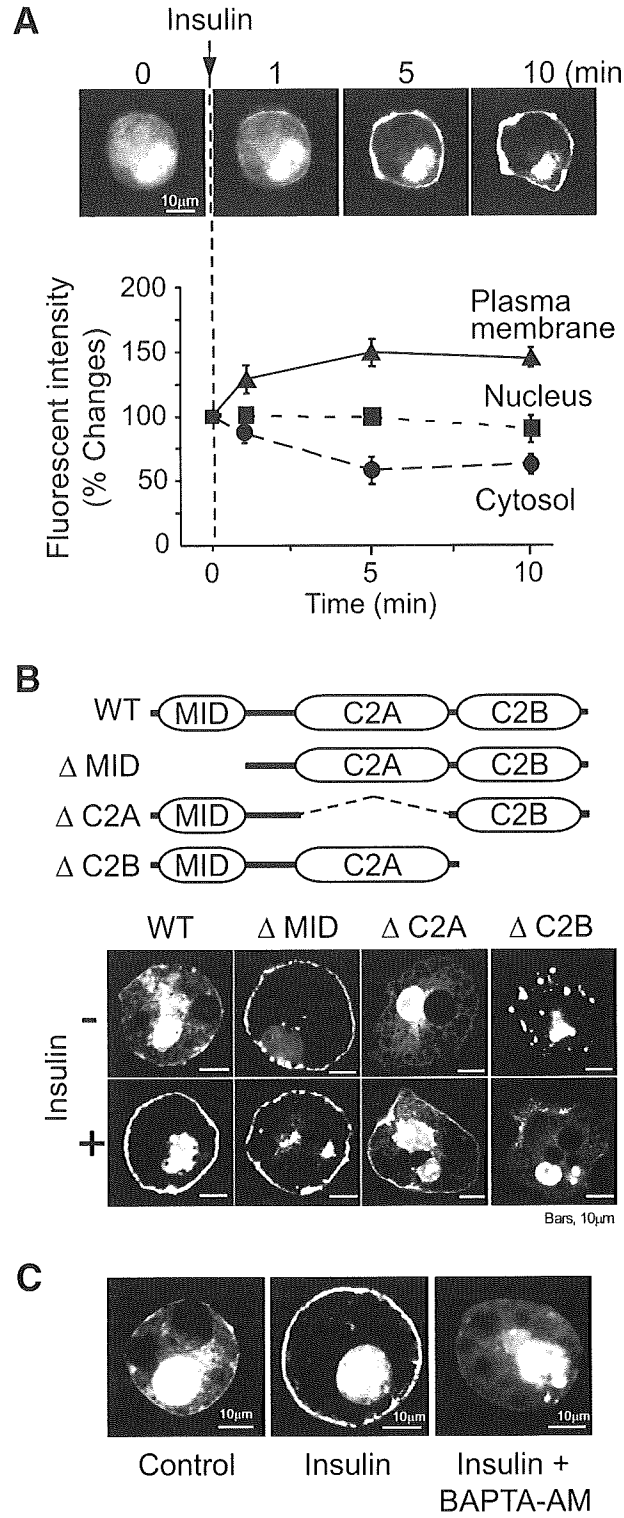

FIG. 2. Insulin augments DOC2b translocation to the plasma membrane. *A*: 3T3-L1 adipocytes were electroporated with eGFP-DOC2b and then treated with 100 nmol/l of insulin for the times indicated. Live fluorescent images of the cells were captured by confocal microscopy. Relative fluorescences of the plasma membrane, nucleus, and cytosol were each measured in three distinct areas. At least three cells were analyzed for each condition. Results are means ± SD from three independent experiments. *B*: 3T3-L1 adipocytes expressing eGFP-DOC2b (WT [wild type], ΔMID, ΔC2A, or ΔC2B) were treated with or without 100 nmol/l of insulin and observed by confocal microscopy. *C*: 3T3-L1 adipocytes were electroporated with eGFP-DOC2b and then pretreated with 50 μmol/l of BAPTA-AM for 10 min, before treatment with insulin and observed under a confocal microscope.

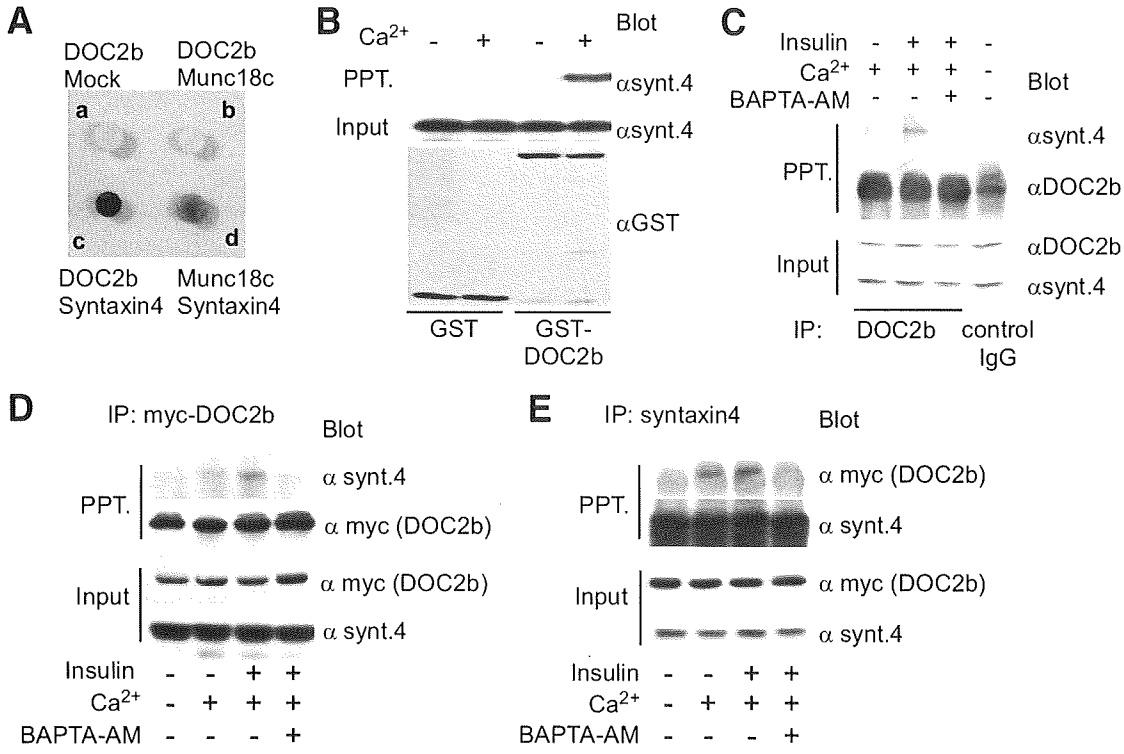

FIG. 3. Insulin promotes Ca^{2+}-dependent interaction between DOC2b and syntaxin-4. *A*: pLexA containing DOC2b or munc18c and pB42AD containing munc18c, syntaxin-4 (synt.4) or empty vectors were coexpressed in the yeast strain of EGY48 (p8op-lacZ), followed by incubation at 30°C for 16 h. Transcriptional activation of LacZ was determined by β-galactosidase assay. *B*: GST-tagged DOC2b and syntaxin-4 were bacterially expressed. Syntaxin-4 protein was cleaved by PreScession protease and further purified with Amicon Ultra filter devices. Both proteins (1 μg each) were mixed in Tris-buffered saline in the presence of 2 mmol/l EDTA or 1 mmol/l $CaCl_2$ and pulled down by glutathione sepharose. The precipitates were analyzed by Western blotting with anti–syntaxin-4 and anti-GST antibodies. *C*: 3T3-L1 adipocytes were serum-starved for 3–4 h and pretreated with or without 50 μmol/l of BAPTA-AM before insulin treatment. The DOC2b–syntaxin-4 interaction was determined by immunoprecipitation using anti-DOC2b antibody. The immunoprecipitated proteins were immunoblotted with anti–syntaxin-4 and anti-DOC2b antibodies. *D* and *E*: Myc-tagged DOC2b was expressed by adenovirus vector in 3T3-L1 adipocytes. After serum starvation and pretreatment with or without 50 μmol/l of BAPTA-AM, before insulin treatment, the cells were stimulated with or without 100 nmol/l of insulin for 20 min and then immunoprecipitated with anti-myc or anti–syntaxin-4 antibodies. The immunoprecipitated proteins were immunoblotted with anti-myc and anti–syntaxin-4 antibodies.

agent BAPTA-AM inhibited insulin-dependent translocation of DOC2b.

DOC2b binds syntaxin-4 upon stimulation with insulin. Since DOC2b is thought to be a soluble calcium-sensing protein, compartment-specific targeting must be achieved through interaction with membrane-bound proteins such as SNARE and SNARE-related proteins. Therefore, we attempted to identify DOC2b-binding partners among these proteins using a yeast two-hybrid system. We found a very strong interaction between DOC2b and syntaxin-4 compared with the already known binding between munc18c and syntaxin4 (Fig. 3*A*). Interestingly, this t-SNARE protein is reportedly a key molecule for GLUT4 vesicle fusion in response to insulin (5,15). Although this interaction was very strong, SNARE proteins are quite "sticky" and can on occasion bind with many proteins nonspecifically. Therefore, we performed the following three additional experiments. First, we determined the direct interaction in vitro using recombinant proteins, GST-tagged DOC2b, and synthesized syntaxin-4. As shown in Fig. 3*B*, the interaction was easily detected by immunoblotting in the presence of calcium. Second, we examined endogenous protein-protein interactions by immunoprecipitation experiments using polyclonal anti-DOC2b. As shown in Fig. 3*C*, insulin treatment increased DOC2b–syntaxin-4 binding, and BAPTA-AM abolished this interaction. Since the molecular weights of DOC2b and the IgG heavy chain are quite similar (computed molecular weight of DOC2b and syntaxin-4 are 46 and 34 kDa, respectively), it was difficult to perform a reverse immunoprecipitation experiment. Third, our results were confirmed by immunoprecipitation experiments using adipocytes expressing myc-tagged DOC2b (Fig. 3*D* and *E*). It is important to note that we could not detect the interaction between DOC2b and syntaxin-4 in the buffer containing EDTA (data not shown). Furthermore, we could not find interaction between DOC2b and syntaxin6 in 3T3-L1 adipocytes (online appendix Fig. S2).

To better assess the calcium dependency of DOC2b translocation and interaction with syntaxin-4 in adipocytes, we conducted the following additional experiments using a Ca^{2+}-unbound mutant. Based on the information from crystallographic analysis of synaptotagmin-1 (16–18), we created mutations in the putative Ca^{2+}-binding sites of DOC2b (i.e., C2A [D157N, D163N] and C2B [D297N, D303N]) and designated the product obtained the CIM (Fig. 4*A*). This type of mutant reportedly loses its calcium-dependent phospholipids-targeting capacity (19,20). As shown in Fig. 4*B*, the CIM mutation markedly inhibited insulin-induced DOC2b translocation. Furthermore, CIM-DOC2b also failed to interact with syntaxin-4 in both the in vivo and the in vitro setting (Fig. 4*C–E*). These results raise the possibility that Ca^{2+} binding is essential for insulin-stimulated DOC2b translocation as well as the interaction with syntaxin-4.

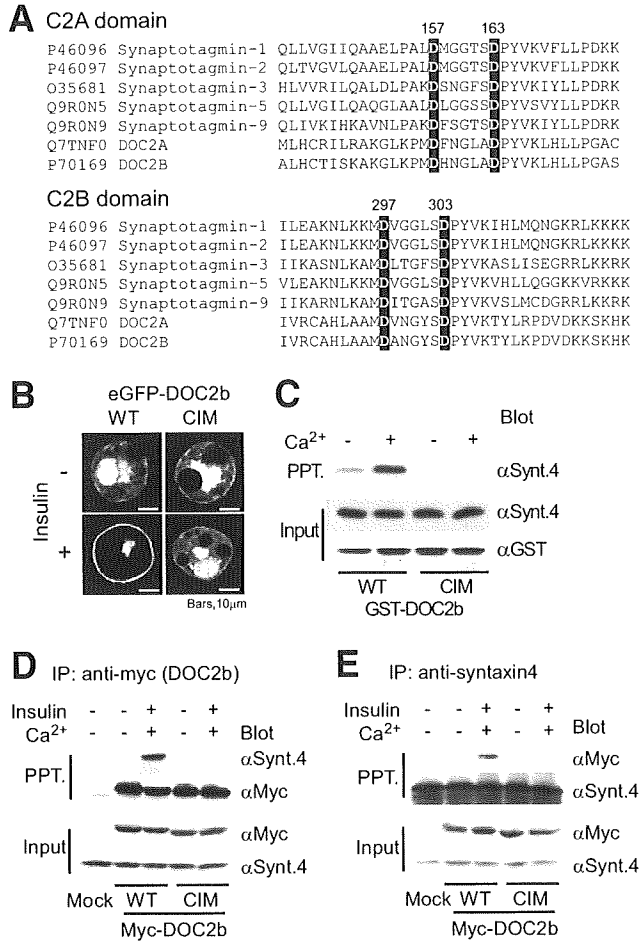

FIG. 4. Calcium binding to DOC2b is essential for its translocation and interaction with syntaxin-4. *A*: **ClustalW sequence alignment of C2A and C2B domains from synaptotagmin-1, -2, -3, -5, and -9 and DOC2a and DOC2b. Two aspartic acid residues in each C2 domain (shown on a black background) are well-conserved putative Ca^{2+}-binding sites. These four aspartic acid residues were mutated into asparagine for CIM-DOC2b (D157N, D163N, D297N, and D303N) construction.** *B*: **Wild-type (WT) or calcium-interacting domain mutants (CIM) of eGFP-DOC2b were expressed in 3T3-L1 adipocytes, which were then treated with insulin and observed under a confocal microscope. Figures show representative images of three independent experiments.** *C*: **Purified GST-DOC2b (WT or CIM) and syntaxin-4 were mixed in the presence of 2 mmol/l EDTA or 1 mmol/l of $CaCl_2$ and pulled down with glutathione sepharose. The precipitates were analyzed by Western blotting with anti–syntaxin-4 and anti-GST antibodies.** *D* **and** *E*: **Myc-tagged DOC2b (WT or CIM) was expressed in 3T3-L1 adipocytes. After serum starvation, the cells were stimulated with or without 100 nmol/l of insulin for 20 min and then immunoprecipitated with anti-myc or anti–syntaxin-4 antibodies. The immunoprecipitated proteins were immunoblotted with anti-myc and anti–syntaxin-4 antibodies.**

DOC2b regulates the step of GLUT4 vesicle fusion in response to insulin. One interpretation of the above findings is that DOC2b may act as a Ca^{2+} sensor protein for SNARE complexes triggering GLUT4 vesicle fusion. To assess the role of DOC2b in GLUT4 vesicle fusion to the plasma membrane, we utilized a GLUT4 construct containing four myc epitopes in the first exofacial loop of GLUT4 and an eGFP fusion at its cytoplasmic COOH terminus. These exofacial tags are easily detected by anti-myc antibody but only when GLUT4 vesicles are fused to the plasma membrane (21). Adipocytes expressing this GLUT4 construct and DsRed2-DOC2b (wild type or CIM) or shRNAs were observed by confocal microscopy. As shown in Fig. 5*A* and *B*, the externalized GLUT4 was increased in the cells coexpressing wild-type DOC2b, while being decreased in those coexpressing CIM-DOC2b or shRNA ($shRNA_{DOC2b}$) compared with the control cells. Since the above conclusions were based on qualitative visual impression, we next estimated the fluorescent signals of the cellular rims in Fig. 5*A* and *B* in two ways. First, we counted the number of the cells with eGFP rims (50 cells in each condition) in the cells expressing myc-GLUT4-eGFP. As shown in Fig. 5*C*, just translocated or docked GLUT4 detected by eGFP fluorescence did not change under either condition. Second, we quantified the ratio of cell surface GLUT4 (myc sinal) to GLUT4 translocated to plasma membrane (eGFP signal) as previously described (22). As shown in Fig. 5*D* and *E*, cell surface GLUT4 was increased in the cells expressing wild-type DOC2b but decreased in those expressing CIM-DOC2b and silenced DOC2b (Fig. 5*D* and *E*). These results, taken together with the data shown in Fig. 5*A*, are consistent with the idea that DOC2b is a calcium-sensing protein and regulates the GLUT4 vesicle fusion step in response to insulin.

Role of DOC2b in glucose transport in 3T3-L1 adipocytes. We next focused on the role of DOC2b in insulin-dependent glucose uptake in adipocytes expressing wild-type DOC2b and CIM-DOC2b. As shown in Fig. 6*A*, overexpression of wild-type DOC2b increased insulin-stimulated glucose uptake to 122% of the control level. In contrast, overexpression of CIM-DOC2b decreased to 78% of the control level. Furthermore, we introduced shRNAs ($shRNA_{DOC2b,\ control}$) by adenovirus vectors into cultured adipocytes to induce specific degradation of the DOC2b mRNA. DOC2b protein expression was decreased to 50 and 10% of the control level in the cells infected with viruses at multiplicity of infection (MOI) of 20 and 50, respectively (Fig. 6*B*). As expected, glucose uptake was decreased from 87 to 60% in adipocytes infected with the adenovirus vectors at MOI of 20–50 (Fig. 6*B*). To confirm the specificity of silencing, we conducted add-back style rescue experiment using adenovirus vector containing wild-type DOC2b. As shown in online appendix Fig. S3, overexpression of DOC2b rescued the inhibitory effect on glucose uptake in DOC2b-silenced cells. Under these conditions, DOC2b overexpression and silencing had no effects on serine phosphorylation of Akt (Fig. 6*A* and *B* and online appendix Fig. S3). These results, taken together with the data presented in Figs. 2–5, suggest that DOC2b regulates glucose transport through modulating vesicle fusion processes but not insulin signaling.

DISCUSSION

Regulation of glucose uptake in muscle and adipose tissues by insulin is of fundamental importance for proper maintenance of postprandial hyperglycemia. This hormone stimulates translocation of the GLUT4 glucose transporter from the intracellular membrane to the cell surface (1,2). In addition to this movement of intracellular vesicles containing GLUT4, it has been suggested that the docking and fusion step of GLUT4 vesicles is also critically regulated by insulin (3,4,23). However, the precise mechanism by which insulin regulates vesicle fusion is still largely unknown.

A key finding of this study is identification of the double C2 domain protein DOC2b, which mediates insulin-regulated GLUT4 vesicle fusion. Like other membrane fusion processes, GLUT4 vesicle fusion occurs essentially through the formation of a "core complex" consisting of syntaxin-4 and VAMP-2 (5). In general, however, a number of additional factors are required to bring about SNARE-mediated membrane fusion in vivo. Many of these factors,

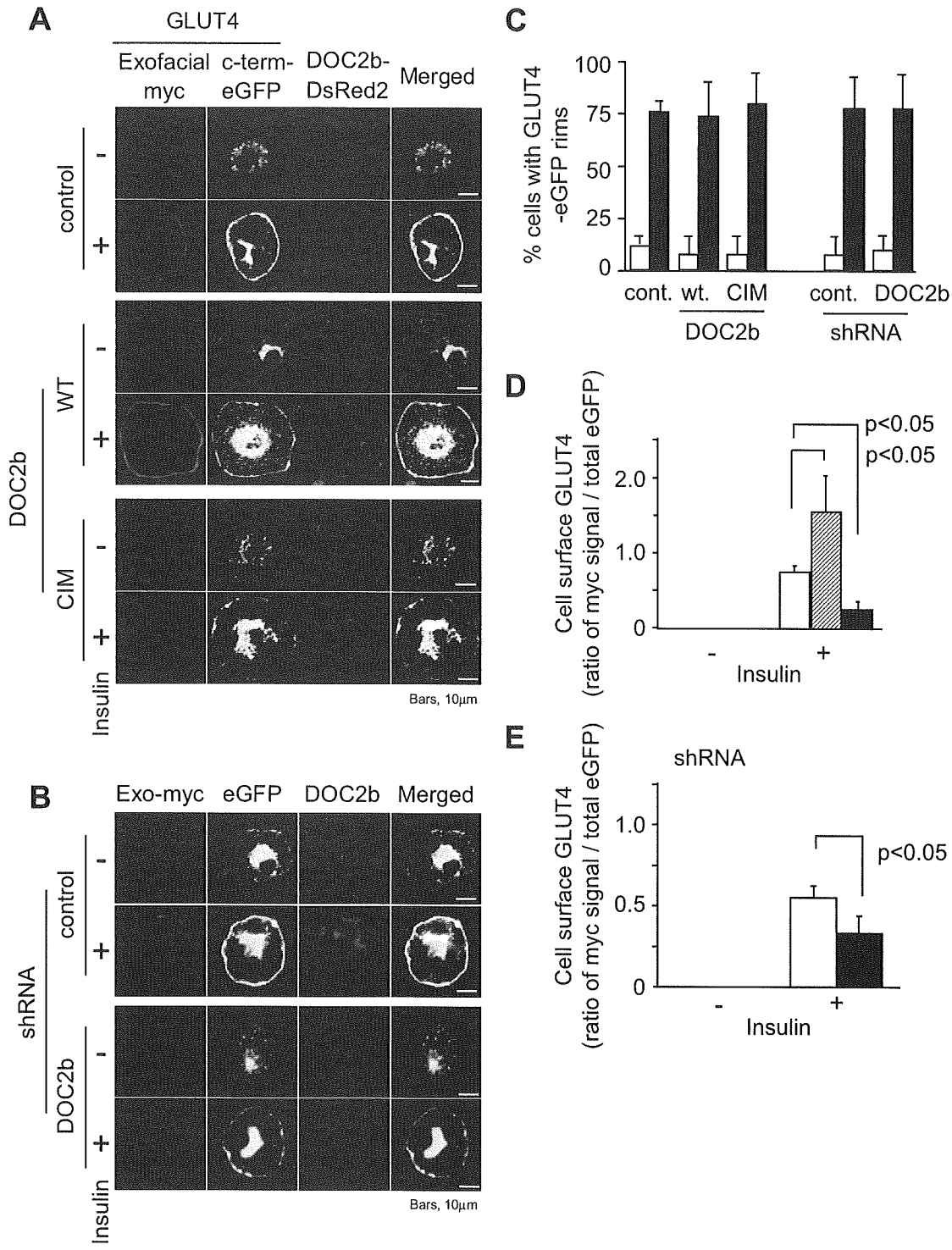

FIG. 5. DOC2b enhances GLUT4 vesicle fusion in 3T3-L1 adipocytes. *A* and *B*: Exofacial myc-tagged GLUT4-eGFP and DsRed2-DOC2b or pcPUR-U6i-shRNA$_{DOC2b,control}$ were coelectroporated into 3T3-L1 adipocytes. The cells were serum starved for 2–4 h and either untreated or treated with 100 nmol/l of insulin for 20 min. The cells were then fixed and stained with anti-myc antibody and Cy5-labeled secondary antibody without detergents. In the cells electroporated with shRNAs, endogenous DOC2b were visualized with anti-DOC2b antibody, followed by Cy3-labeled secondary antibody. Stained cells were observed by confocal microscopy. This shRNA system decreased DOC2b protein expression to 10–20% of control level. Images are representative of three independent experiments. *C–E*: Percents of cells with GLUT4-eGFP rims and the cell surface myc-GLUT4 contents (the ratio of myc signal/eGFP signal at plasma membrane rims) in Fig. 5*A* was calculated as described under RESEARCH DESIGN AND METHODS. *C*: □, −insulin; ■, +insulin. *D*: □, control; ▨, wild type; ■, CIM. E: □, shRNA control; ■, shRNA DOC2b. The graphs represent values from at least 3–5 independent experiments, and error bars show SD. (Please see http://dx.doi.org/10.2337/db08-0303 for a high-quality digital representation of this figure.)

which can collectively be called SNARE regulators (e.g., munc18, synaptotagmin, munc13, GATE-16/Apg8, LMA1, synaptophysin, tomosyn, and Vsm1/Ddi1), bind directly to SNARE proteins and are involved in membrane trafficking and fusion events (24). Among these SNARE regulators, munc18c and tomosyn were reported to be negative regulators of the SNARE complex assembly involved in GLUT4 vesicle fusion (25–27). Despite numerous investigations, the positive SNARE regulators for GLUT4 vesicle fusion have not been adequately clarified. In this report, we have shown that

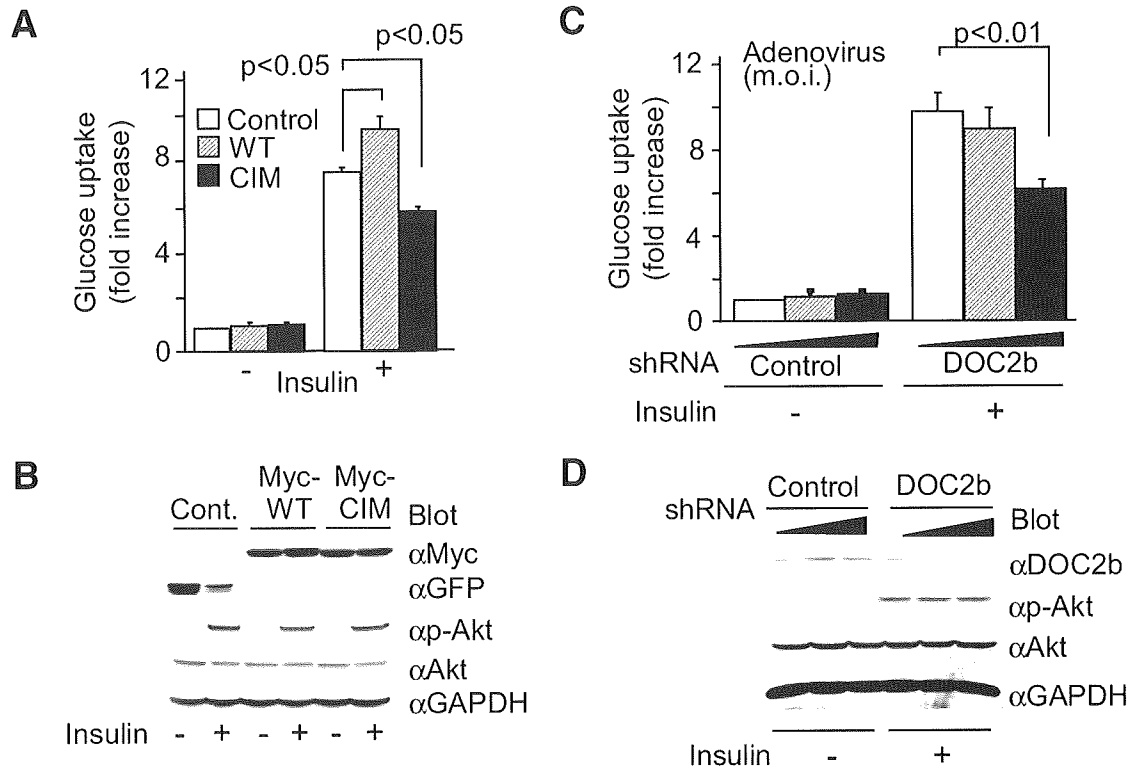

FIG. 6. DOC2b regulates insulin-stimulated glucose uptake in 3T3-L1 adipocytes. 3T3-L1 adipocytes were infected with recombinant adenovirus vectors encoding eGFP, myc-tagged DOC2b (WT, CIM) at MOI of 50 (*A* and *B*) or adenovirus vectors encoding shRNA specific for DOC2b or nontargeting control at MOI of 0, 20, and 50 (*C* and *D*). After serum starvation, the cells were treated with or without 100 nmol/l of insulin for 10 min. *A*: □, control; ▨ wild type;; ■, CIM. *C*: □, 0; ▨, 20; ■, 50. 2-Deoxy-glucose uptake was measured under each condition. Results are presented as means ± SD of at least five independent experiments. *B* and *D*: The cell lysates were also immunoblotted with anti-myc, anti-GFP, anti-DOC2b, anti-Akt, anti–phosphoserine-Akt, and anti–glyceraldehyde-3-phosphate dehydrogenase antibodies. Immunoblots were representative of at least three independent experiments.

DOC2b mediates insulin-stimulated GLUT4 membrane fusion in adipocytes, while having no effect on the GLUT4 vesicle translocation step. These data are consistent with the hypothesis that DOC2b regulates insulin-stimulated GLUT4 vesicle fusion. DOC2b may be a positive SNARE regulator for vesicle fusion processes in adipocytes.

A second significant finding reported herein is the identification of a DOC2b binding partner. DOC2b interacts with t-SNARE syntaxin-4 upon stimulation with insulin in the presence of calcium. Syntaxin-4 is thought to be a SNARE protein on the target membrane for GLUT4 vesicle fusion (28,29). As shown in Fig. 3*A*, this interaction appears to be very strong compared with that between munc18c and syntaxin-4 demonstrated by the yeast two-hybrid method. Although this interaction appeared to be very strong, SNARE proteins are quite sticky and can on occasion bind with many proteins nonspecifically. Therefore, we performed three additional experiments. As shown in Fig. 3*B–E*, we confirmed the interaction between DOC2b and syntaxin-4 in both the in vivo and the in vitro setting. Furthermore, changes in the intracellular localization of DOC2b also supported the functional interaction. As shown in Fig. 2*A*, DOC2b translocates to the plasma membrane in response to insulin stimulation. Importantly, the time scale of DOC2b translocation coincides with relatively slow externalization of GLUT4 vesicles. Taken together, our data are consistent with the aforementioned hypothesis that DOC2b regulates GLUT4 vesicle fusion by triggering SNARE complex assembly.

Another interesting observation made in this study is the essential role of $[Ca^{2+}]i$ in insulin-stimulated GLUT4 vesicle fusion. In 2001, Whitehead et al. (8) first reported that a calcium chelator, BAPTA-AM, inhibited GLUT4 externalization and glucose uptake. However, the precise mechanism underlying calcium-dependent GLUT4 vesicle fusion remains unknown because no studies have as yet focused on Ca^{2+}-sensing proteins in adipocytes. DOC2b is structurally similar to the well-known calcium-sensing SNARE regulator synaptotagmins (Fig. 4*A*). Taking these observations together, we hypothesized that DOC2b is a Ca^{2+}-sensing protein that regulates GLUT4 vesicle fusion in adipocytes. To better assess the role of Ca^{2+} in GLUT4 vesicle fusion, we confirmed the following. First, DOC2b translocation and its binding to syntaxin-4 were shown to be $[Ca^{2+}]i$ dependent. Second, mutations in calcium-binding sites on C2 domains of DOC2b resulted in loss of syntaxin-4 binding, GLUT4 externalization, and glucose uptake. In contrast, we also observed DOC2b–syntaxin-4 binding, without insulin action, in a GST pull-down assay, suggesting that $[Ca^{2+}]i$ is necessary for this interaction in vitro (Fig. 3*B*). In parallel, we also found that insulin initiates the DOC2b translocation to plasma membrane and promotes interaction between DOC2b and syntaxin-4 in the presence of Ca^{2+} ions. Based on the above observations, we propose a simple model whereby insulin regulates SNARE regulator DOC2b, and basal level of $[Ca^{2+}]i$ may act in a constitutive manner to promote DOC2b–syntaxin-4 interaction involved in insulin-stimulated GLUT4 vesicle fusion.

A recent report (30) suggests that DOC2 proteins remove munc18 from syntaxin, thereby regulating core SNARE complex formation. This interpretation is very attractive because munc18c is thought to be a negative regulator of GLUT4 vesicle fusion. Although we have no direct data pertaining to

munc18c, it is possible that munc18c and DOC2b may modulate SNARE assembly in a counterregulatory manner. Very recently, Ke et al. (31) reported that DOC2b bound munc18c, but not syntaxin-4, in pancreatic β-cells. This apparent discrepancy on syntaxin-4 binding may be attributable to the different experimental conditions. They performed most of their experiments using a buffer without calcium (i.e., Nonidet P-40 lysis buffer). Since DOC2b has conserved Ca^{2+}-binding sites and is thought to be a Ca^{2+} sensor protein in other cell types such as neuron (32) and chromaffin cells (33), Ca^{2+} might be important for the physiological properties of DOC2b in β-cells. Further work is required to uncover the underling mechanisms by which DOC2b regulates SNARE assembly in response to insulin.

In summary, we have identified DOC2b as a syntaxin-4 binding protein in adipocytes. This protein regulates GLUT4 vesicle fusion as well as glucose uptake in response to insulin stimulation. We have further revealed that DOC2b requires $[Ca^{2+}]i$ and positively regulates the step of GLUT4 vesicle fusion.

ACKNOWLEDGMENTS

This work was partly supported by grants-in-aid for scientific research from the Ministry of Education, Culture, Sports, Science, and Technology of Japan (to M.E. and Y.T.); from the Takeda Scientific Foundation (to M.E.); and by the Research Grant for Longevity Science (to Y.T.).

No potential conflicts of interest relevant to this article were reported.

We thank Dr. R.R. Duncan for the DOC2a,b constructs, Dr. T. Takuma for the munc18c construct, Dr. K. Taira for the pcPUR+U6i cassette, and Dr. M. Fukuda for the anti-DOC2b antibody. We are also very grateful to Dr. Teruo Nishida for generously supporting us in the experiments using the confocal microscope and to Y. Kora, M. Kaneko, K. Yamada, and S. Ota for their technical supports.

REFERENCES

1. Yang J, Holman, GD: Comparison of GLUT4 and GLUT1 subcellular trafficking in basal and insulin-stimulated 3T3-L1 cells. *J Biol Chem* 268:4600–4603, 1993
2. Czech MP, Corvera S: Signaling mechanisms that regulate glucose transport. *J Biol Chem* 274:1865–1868, 1999
3. Koumanov F, Jin B, Yang J, Holman GD: Insulin signaling meets vesicle traffic of GLUT4 at a plasma-membrane-activated fusion step. *Cell Metab* 2:179–189, 2005
4. Gonzalez E, McGraw TE: Insulin signaling diverges into Akt-dependent and -independent signals to regulate the recruitment/docking and the fusion of GLUT4 vesicles to the plasma membrane. *Mol Biol Cell* 17:4484–4493, 2006
5. Cheatham B, Chuk AV, Kahn CR, Wang L, Rhodes CJ, Klip A: Insulin-stimulated translocation of GLUT4 glucose transporters requires SNARE-complex proteins. *Proc Natl Acad Sci U S A* 93:15169–15173, 1996
6. Burgoyne RD, Morgan A: Secretory granule exocytosis. *Physiol Rev* 83:581–632, 2003
7. Tucker WC, Weber T, Chapman ER: Reconstitution of Ca^{2+}-regulated membrane fusion by synaptotagmin and SNAREs. *Science* 304:435–438, 2004
8. Whitehead JP, Molero JC, Clark S, Meneilly MS, James DE: The role of Ca^{2+} in insulin-stimulated glucose transport in 3T3-L1 cells. *J Biol Chem* 276:27816–27824, 2001
9. Perin MS, Fried VA, Mignery GA, Jahn R, Sudhof TC: Phospholipid binding by a synaptic vesicle protein homologous to the regulatory region of protein kinase C. *Nature* 345:260–263, 1990
10. Rickman C, Craxton M, Osborne S, Davletov B: Comparative analysis of tandem C2 domains from the mammalian synaptotagmin family. *Biochem J* 378:681–686, 2004
11. Miyagishi M, Taira K: U6 promoter-driven siRNAs with four uridine 3′ overhangs efficiently suppress targeted gene expression in mammalian cells. *Nat Biotechnol* 20:497–500, 2002
12. Kuroda TS, Fukuda M: Rab27A-binding protein Slp2-a is required for peripheral melanosome distribution and elongated cell shape in melanocytes. *Nat Cell Biol* 6:1195–1203, 2004
13. Hui E, Bai J, Wang P, Sugimori M, Llinas RR, Chapman ER: Three distinct kinetic groupings of the synaptotagmin family: candidate sensors for rapid and delayed exocytosis. *Proc Natl Acad Sci U S A* 102:5210–5214, 2005
14. Fukuda M, Saegusa C, Kanno E, Mikoshiba K: The C2A domain of double C2 protein γ contains a functional nuclear localization signal. *J Biol Chem* 276:24441–24444, 2001
15. Volchuk A, Wang Q, Ewart HS, Liu Z, He L, Bennett MK, Klip A: Syntaxin 4 in 3T3-L1 adipocytes: regulation by insulin and participation in insulin-dependent glucose transport. *Mol Biol Cell* 7:1075–1082, 1996
16. Sutton RB, Davltov BA, Berghuis AM, Sudhof TC, Sprang S: Structure of the first C2 domain of synaptotagmin I: a novel Ca^{2+}/phospholipid-binding fold. *Cell* 80:929–938, 1995
17. Shao X, Davletov BA, Sutton RB, Sudhof TC, Rizo J: Bipartite Ca^{2+}-binding motif in C2 domains of synaptotagmin and protein kinase C. *Science* 273:248–251, 1996
18. Fernandez I, Arac D, Ubach J, Gerber SH, Shin O, Gao Y, Anderson R, Sudhof TC, Rizo J: Three-dimensional structure of the synaptotagmin 1 C2B-domain: synaptotagmin 1 as a phospholipid binding machine. *Neuron* 32:1057–1069, 2001
19. Fukuda M, Kojima T, Mikoshiba K: Regulation by bivalent cations of phospholipid binding to the C2A domain of synaptotagmin III. *Biochem J* 323:421–425, 1997
20. Mackler JM, Drummond JA, Loewen CA, Robinson IM, Reist NE: The C_2B Ca^{2+}-binding motif of synaptotagmin is required for synaptic transmission in vivo. *Nature* 418:340–344, 2002
21. Bogan JS, McKee AE, Lodish HF: Insulin-responsive compartments containing GLUT4 in 3T3-L1 and CHO cells: regulation by amino acid concentrations. *Mol Cell Biol* 21:4785–4806, 2001
22. Park JG, Bose A, Leszyk J, Czech MP: PYK2 as a mediator of endothelin-1/G alpha 11 signaling to GLUT4 glucose transporters. *J Biol Chem* 276:47751–47754, 2001
23. Lizunov VA, Matsumoto H, Zimmerberg J, Cushman SW, Frolov VA: Insulin stimulates the halting, tethering, and fusion of mobile GLUT4 vesicles in rat adipose cells. *J Cell Biol* 169:481–489, 2005
24. Gerst JE: SNARE regulators: matchmakers and matchbreakers. *Biochim Biophys Acta* 1641:99–110, 2003
25. Thurmond DC, Ceresa BP, Okada S, Elemendorf JS, Coker K, Pessin JE: Regulation of insulin-stimulated GLUT4 translocation by Munc18c in 3T3-L1 adipocytes. *J Biol Chem* 273:33876–33883, 1998
26. Kanda H, Tamori Y, Shinoda H, Yoshikawa M, Sakaue M, Udagawa J, Otani H, Tashiro F, Miyazaki J, Kasuga M: Adipocytes from Munc18c-null mice show increased sensitivity to insulin-stimulated GLUT4 externalization. *J Clin Invest* 115:291–301, 2005
27. Widberg CH, Bryant NJ, Girotti M, Res S, James DE: Tomosyn interacts with the t-SNAREs syntaxin4 and SNAP23 and plays a role in insulin-stimulated GLUT4 translocation. *J Biol Chem* 278:35093–35101, 2003
28. Tellam JT, Macaulay SL, Mcintosh S, Hewish DR, Ward CW, James DE: Characterization of munc-18c and syntaxin-4 in 3T3-L1 adipocytes. *J Biol Chem* 272:6179–6186, 1997
29. Yang C, Coker KJ, Kim JK, Mora S, Thurmond DC, Davis AC, Yang B, Williamson RA, Shulman GI, Pessin JE: Syntaxin 4 heterozygous knockout mice develop muscle insulin resistance. *J Clin Invest* 107:1311–1318, 2001
30. Verhage M, de Vries KJ, Roshol H, Burbach JP, Gispen WH, Sudhof TC: DOC2 proteins in rat brain: complementary distribution and proposed function as vesicular adapter proteins in early stages of secretion. *Neuron* 18:453–461, 1997
31. Ke B, Oh E, Thurmond DC: Doc2beta is a novel munc18c-interacting partner and positive effector of syntaxin 4-mediated exocytosis. *J Biol Chem* 282:21786–21797, 2007
32. Groffen AJ, Friedrich R, Brian EC, Ashery U, Verhage M: DOC2A and DOC2B are sensors for neuronal activity with unique calcium-dependent and kinetic properties. *J Neurochem* 97:818–833, 2006
33. Friedrich R, Groffen AJ, Connell E, van Weering JR, Gutman O, Henis YI, Davletov B, Ashery U: DOC2B acts as a calcium switch and enhances vesicle fusion. *J Neurosci* 28:6794–6806, 2008

Diabetologia (2009) 52:653–663
DOI 10.1007/s00125-009-1270-6

ARTICLE

Increased insulin demand promotes while pioglitazone prevents pancreatic beta cell apoptosis in *Wfs1* knockout mice

M. Akiyama · M. Hatanaka · Y. Ohta · K. Ueda · A. Yanai · Y. Uehara · K. Tanabe · M. Tsuru · M. Miyazaki · S. Saeki · T. Saito · K. Shinoda · Y. Oka · Y. Tanizawa

Received: 7 May 2008 / Accepted: 29 December 2008 / Published online: 4 February 2009

Abstract
Aims/hypothesis The *WFS1* gene encodes an endoplasmic reticulum (ER) membrane-embedded protein called Wolfram syndrome 1 protein, homozygous mutations of which cause selective beta cell loss in humans. The function(s) of this protein and the mechanism by which the mutations of this gene cause beta cell death are still not fully understood. We hypothesised that increased insulin demand as a result of obesity/insulin resistance causes ER stress in pancreatic beta cells, thereby promoting beta cell death.
Methods We studied the effect of breeding *Wfs1*$^{-/-}$ mice on a C57BL/6J background with mild obesity and insulin resistance, by introducing the agouti lethal yellow mutation (*A*^{y}*/a*). We also treated the mice with pioglitazone.
Results *Wfs1*$^{-/-}$ mice bred on a C57BL/6J background rarely develop overt diabetes by 24 weeks of age, showing only mild beta cell loss. However, *Wfs1*$^{-/-}$ *A*^{y}*/a* mice developed selective beta cell loss and severe insulin-deficient diabetes as early as 8 weeks. This beta cell loss was due to apoptosis. In *Wfs1*$^{+/+}$ *A*^{y}*/a* islets, levels of ER chaperone immunoglobulin-binding protein (BiP)/78 kDa glucose-regulated protein (GRP78) and phosphorylation of eukaryotic translation initiation factor 2, subunit α (eIF2α) apparently increased. Levels of both were further increased in *Wfs1*$^{-/-}$ *A*^{y}*/a* murine islets. Electron micrography revealed markedly dilated ERs in *Wfs1*$^{-/-}$ *A*^{y}*/a* murine beta cells. Interestingly, pioglitazone treatment protected beta cells from apoptosis and almost completely prevented diabetes development.

Electronic supplementary material The online version of this article (doi:10.1007/s00125-009-1270-6) contains supplementary material, which is available to authorised users.

M. Akiyama · M. Hatanaka · Y. Ohta · K. Tanabe · M. Tsuru · M. Miyazaki · Y. Tanizawa (✉)
Division of Endocrinology, Metabolism, Hematological Sciences and Therapeutics, Department of Bio-Signal Analysis, Yamaguchi University Graduate School of Medicine, 1-1-1 Minami Kogushi, Ube, Yamaguchi 755-8505, Japan
e-mail: tanizawa@yamaguchi-u.ac.jp

K. Ueda
Health Service Center, Organization for University Education, Yamaguchi University, Ube, Yamaguchi, Japan

A. Yanai · K. Shinoda
Division of Neuroanatomy, Department of Neuroscience, Yamaguchi University Graduate School of Medicine, Ube, Yamaguchi, Japan

Y. Uehara · S. Saeki · T. Saito
Applied Medical Engineering Science, Yamaguchi University Graduate School of Medicine, Ube, Yamaguchi, Japan

K. Tanabe
The Japan Health Science Foundation, Tokyo, Japan

Y. Oka
Division of Molecular Metabolism and Diabetes, Department of Internal Medicine, Tohoku University Graduate School of Medicine, Sendai, Japan

Conclusions/interpretation *Wfs1*-deficient beta cells are susceptible to ER stress. Increased insulin demand prompts apoptosis in such cells in vivo. Pioglitazone, remarkably, suppresses this process and prevents diabetes. As common *WFS1* gene variants have recently been shown to confer a risk of type 2 diabetes, our findings may be relevant to the gradual but progressive loss of beta cells in type 2 diabetes.

Keywords Apoptosis · Diabetes mellitus · Endoplasmic reticulum · Endoplasmic reticulum stress · Insulin · Pancreatic beta cell · Pioglitazone · Wolfram syndrome

Abbreviations

eIF2α	Eukaryotic translation initiation factor 2,subunit α
ER	Endoplasmic reticulum
GRP78	78 kDa Glucose-regulated protein
GRP94	94 kDa Glucose-regulated protein
ipGTT	Intraperitoneal glucose tolerance test
IRE1	Inositol-requiring protein 1
ITT	Insulin tolerance test
UPR	Unfolded protein response
WFS1	Wolfram syndrome 1
WT	Wild-type

Introduction

Many obese individuals with marked insulin resistance do not develop overt diabetes. However, in individuals destined to develop type 2 diabetes, pancreatic beta cells fail to produce enough insulin to meet systemic demand. This beta cell failure is caused by insufficient beta cell response to glucose and inadequate beta cell mass expansion [1]. Recently, several reports have convincingly confirmed the contribution of beta cell mass reduction to type 2 diabetes [2, 3], at least in its advanced stages. Although the cause of this decrease is unknown, increased apoptosis may play an important role [1, 2]. In addition to genetic factors, processes involving glucotoxicity and/or lipotoxicity are likely to be contributory [4]. Endoplasmic reticulum (ER) stress has also recently emerged as a candidate mechanism [5–7].

Wolfram syndrome is a rare recessively inherited genetic disorder, characterised by juvenile-onset diabetes mellitus and progressive optic atrophy [8]. Several neuro-psychiatric illnesses may also be present [9]. Beta cells are selectively lost from the pancreatic islets and this loss is genetically programmed [10]. Our group and others previously identified the Wolfram syndrome gene, designating it *WFS1* [11] or wolframin [12] and showing that it is localised primarily in the ER [13, 14]. Homozygous *Wfs1* knockout mice developed glucose intolerance. However, the diabetic phenotype of the $Wfs1^{-/-}$ mouse was milder than that seen in Wolfram syndrome patients and was largely dependent on genetic background [15].

Despite intensive studies, the precise function of the Wolfram syndrome 1 (WFS1) protein is still largely unknown. It may regulate ER calcium homeostasis by serving as an ER cation channel [16, 17]. Recently the WFS1 protein was also suggested to be a putative chaperone for the Na/K ATPase b1 subunit in the ER [18]. However, it is certain that its function is closely related to ER stress responses. ER stress induces *Wfs1* expression and, in turn, loss of WFS1 protein exacerbates ER stress [15, 19–21]. Furthermore, $Wfs1^{-/-}$ islet cells are susceptible to ER stress-induced apoptosis [15, 21, 22]. ER stress is induced under conditions such as overload of protein synthesis/processing, accumulation of structurally abnormal proteins, disturbance of post-translational modification and ER calcium homeostasis abnormalities. When ER stress develops, cells respond by unfolded protein response (UPR), facilitating protein folding via the induction of chaperone proteins, attenuation of translations, as well as degradation of misfolded proteins, a process called ER-associated degradation [23–25]. If the stress is severe, apoptosis is induced. Accumulating evidence suggests that a high level of ER stress or defective ER stress signalling causes beta cell death and that diabetes thereby develops [26–30].

We wished to test in vivo the hypothesis that beta cell loss in $Wfs1^{-/-}$ mice is caused by an inability to cope with ER stress. The agouti yellow (A^y/a) mouse is a genetic model of mild obesity/insulin resistance with compensatory beta cell hyperplasia [31]. In this mouse, ectopically expressed agouti protein promotes food intake and weight gain by antagonising signalling at melanocortin-4 receptor in the hypothalamus. ER stress is likely to have been induced in these beta cells by increased insulin synthesis and secretion demands, and also by elevated serum NEFA [32]. As $Wfs1^{-/-}$ mice on the C57BL/6J background rarely develop overt diabetes by 24 weeks, we introduced the A^y mutation into C57BL/6J $Wfs1^{-/-}$ mice and assessed the consequences. Furthermore, we treated $Wfs1^{-/-}$ mice with pioglitazone, which ameliorates insulin resistance.

Methods

Animals All experimental protocols were approved by the Ethics of Animal Experimentation Committee at Yamaguchi University School of Medicine.

The $Wfs1^{-/-}$ mice had a C57BL/6J background [15]. The Agouti yellow mice (C57BL/6J*HamSlc-A*^{y}) were obtained from M. Nishimura (Nagoya University Graduate School of Medicine, Nagoya, Japan) and Japan SLC

(Hamamatsu, Japan). We used male mice for all experiments. The mice were kept under standard, specific pathogen-free conditions with a constant dark/light cycle and free access to standard mouse chow (MF; Oriental Yeast, Tokyo, Japan) and water. The high-fat diet (rodent diet with 60% energy from fat; D12492) was purchased from Research Diet (New Brunswick, NJ, USA) and was freely accessible. For pioglitazone treatment, mice were fed standard mouse chow with 0.01% pioglitazone (wt/wt) from the age of 4 weeks. Pioglitazone was provided by Takeda Pharmaceutical (Osaka, Japan).

Generation of $Wfs1^{-/-}$ A^{v}/a mice To generate A^{v}/a mice lacking the *Wfs1* gene, $Wfs1^{-/-}$ mice were bred with A^{v}/a mice to create the compound heterozygote ($Wfs1^{+/-}$ A^{v}/a). This heterozygote was bred with $Wfs1^{+/-}$ *a/a*, and $Wfs1^{-/-}$ A^{v}/a, $Wfs1^{+/+}$ A^{v}/a, $Wfs1^{-/-}$ *a/a* and $Wfs1^{+/+}$ *a/a* (wild-type [WT]) offspring were identified.

The *Wfs1* genotype was determined by PCR. We used the sense primer 5′-CCCAGTTCTTGCTTTACCAC CAGG-3′ and the anti-sense primers 5′-GCCTTCTTGAC GAGTTCTTCTGA-3′ (derived from the neomycin resistance gene) and 5′-ACTTCGTCCAGCACTGGGGTCAG-3′ (derived from the *Wfs1* gene). A^{v}/a mice were identified by coat colour.

Physiological studies Body weights were measured weekly. Blood samples were collected from the tail vein. Non-fasting blood glucose was measured by the glucose oxidase method using a GlucoCard device (Arkray, Kyoto, Japan). Serum insulin levels were determined using an insulin ELISA kit (Morinaga Institute of Biological Science, Tokyo, Japan). Serum triacylglycerol was measured by high-performance liquid chromatography at Skylight Biotech (Akita, Japan), according to the procedure described by Usui et al. [33]. Intraperitoneal glucose tolerance test (ipGTT) and insulin tolerance test (ITT) were performed at 8 weeks of age.

Pancreatic insulin content Pancreases were removed and homogenised in acid/ethanol (0.7 mol/l HCl/ethanol 25:75 plus 0.1% Triton X-100 (vol./vol.)) and left at 4°C for 48 h, with sonication every 24 h. Homogenates were then centrifuged (3,000 *g* for 15 min) and the insulin content of the acid/ethanol supernatant fraction was measured using insulin ELISA. Protein in tissue extracts was determined using the BCA protein assay reagent.

Immunostaining and morphometry Formalin-fixed paraffin-embedded sections were de-paraffinised and re-hydrated, then incubated with primary antibodies. For immunofluorescent staining, appropriate FITC-conjugated or Cy3-conjugated anti-IgG was used. Detailed antibody information is given in the Electronic supplementary material (ESM). Immunohistochemical analyses were performed, with at least three animals for each condition being killed for the purpose. For measurement of beta cell area, more than five pancreatic tissue sections per animal were randomly selected and stained with anti-insulin IgG/3,3′-diaminobenzidine tetrahydrochloride and haematoxylin. Microscopic photoimages were taken with a charge-coupled device (CCD) camera and the pancreatic and beta cell areas were each estimated using a computer program (Y. Uehara, S. Saeki and S. Saito S unpublished results).

Tissue preparation and electron microscopy All animals were anaesthetised with sodium pentobarbital (65 mg/kg, i.p.) and intracardially perfused with 2% glutaraldehyde (vol./vol.) and 4% paraformaldehyde (vol./vol.) in 0.1 mol/l phosphate buffer (pH 7.4) containing 0.2% picric acid (vol./vol.). Pancreatic sections (1 mm thick) were post-fixed with 1% OsO_4 (wt/vol.), block-stained with 2% uranyl acetate (wt/vol.), dehydrated, infiltrated with propylene oxide, placed in a mixture of propylene oxide and Epoxy resin (1:1), and flat-embedded on siliconised glass slides in Epoxy resin. Ultrathin sections were made and mounted on to copper grids. To enhance contrast, they were double stained with 2% uranyl acetate (wt/vol.) and 1% lead citrate (wt/vol.), and observed with a Hitachi H-7500 electron microscope (Hitachi High-Technologies, Tokyo, Japan) operating at 80 kV.

Mouse islet isolation and immunoblotting analysis Pancreatic islets were isolated as described previously [15]. For immunoblotting [34], approximately 100 islets from two to six mice were pooled, then immediately dissolved in lysis buffer containing 1% SDS (50 mmol/l Tris–HCl [pH 6.8], 1% SDS [wt/vol.], 10% glycerol [wt/vol.] and 50 mmol/l dithiothreitol). Anti-WFS1 (N-terminus) antibody has been described previously [15]. For information on other antibodies, see ESM.

Statistical analysis Results are expressed as means±SE. Differences between means were evaluated using ANOVA or Student's *t* test as appropriate. Differences were considered significant at $p<0.05$.

Results

Characteristics of the mice Body weights were monitored weekly beginning at 4 weeks of age. A^{v}/a mice ($Wfs1^{+/+}$ A^{v}/a) were mildly, but significantly more obese than WT littermates ($Wfs1^{+/+}$ *a/a*) by 6 weeks of age (23.5±0.7 vs 21.5± 0.5 g; $p<0.05$). Similarly, $Wfs1^{-/-}$ A^{v}/a mice were also more obese than $Wfs1^{-/-}$ *a/a* mice by 6 weeks of age (23.9±0.3 vs 20.6±0.2 g; $p<0.0001$). However, $Wfs1^{-/-}$ A^{v}/a mice had

lost their excess weight by 17 weeks of age (Fig. 1a). This is attributable to the development of overt diabetes due to severe insulin deficiency (Fig. 1b, c). In fact, non-fasted blood glucose levels of *Wfs1*$^{-/-}$ *A*^{y}*/a* mice started to rise significantly from the age of 8 weeks, with all *Wfs1*$^{-/-}$ *A*^{y}*/a* mice developing overt diabetes by 16 weeks of age (Fig. 1b). Ketosis manifested after age 16 weeks (data not shown). In contrast, blood glucose levels of *Wfs1*$^{+/+}$ *A*^{y}*/a* and *Wfs1*$^{-/-}$ *a/a* mice did not differ from those of WT mice. We also examined plasma insulin levels of these mice. At 12 weeks of age, the plasma insulin levels of *Wfs1*$^{+/+}$ *A*^{y}*/a* mice were significantly higher than those of WT littermates, and *Wfs1*$^{-/-}$ *a/a* and *Wfs1*$^{-/-}$ *A*^{y}*/a* mice. Interestingly, *Wfs1*$^{-/-}$ *A*^{y}*/a* mice tended to be more hyperinsulinaemic than *Wfs1*$^{-/-}$ *a/a* and WT at this age, although the differences did not reach statistical significance. However, at 24 weeks of age, plasma insulin levels in *Wfs1*$^{-/-}$ *A*^{y}*/a* mice were markedly decreased (Fig. 1c).

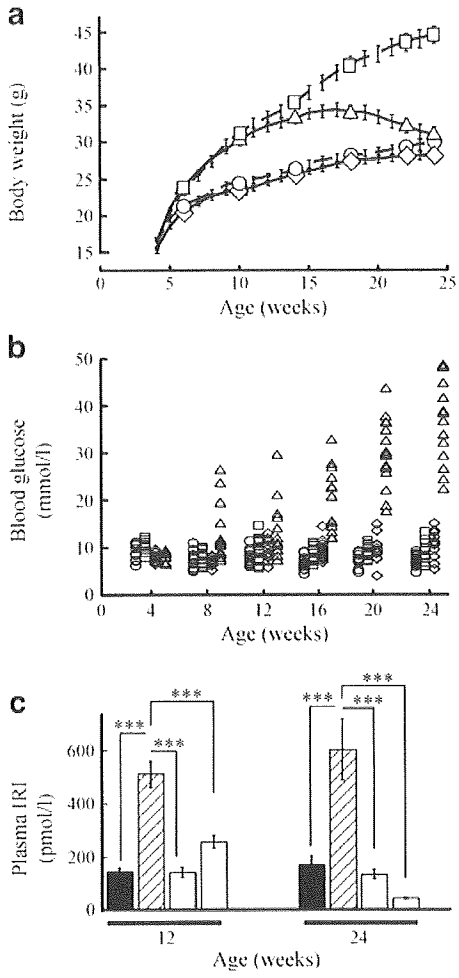

Fig. 1 Weight, blood glucose and insulin levels of *Wfs1*$^{-/-}$ *A*^{y}*/a* and other mice. **a** Weight of *Wfs1*$^{-/-}$ *A*^{y}*/a* (triangles), *Wfs1*$^{+/+}$ *A*^{y}*/a* (squares), *Wfs1*$^{-/-}$ *a/a* (diamonds) and *Wfs1*$^{+/+}$ *a/a* (WT, circles) mice over the course of 24 weeks. Values are the means±SE for n=14–21 mice. **b** Non-fasted blood glucose levels in *Wfs1*$^{-/-}$ *A*^{y}*/a*, *Wfs1*$^{+/+}$ *A*^{y}*/a*, *Wfs1*$^{-/-}$ *a/a* and WT mice; key as above, n=11–16. $p<0.05$ for *Wfs1*$^{-/-}$ *A*^{y}*/a* vs *Wfs1*$^{+/+}$ *A*^{y}*/a*, *Wfs1*$^{-/-}$ *a/a* and WT mice at 8 and 12 weeks; $p<0.001$ for *Wfs1*$^{-/-}$ *A*^{y}*/a* vs *Wfs1*$^{+/+}$ *A*^{y}*/a*, *Wfs1*$^{-/-}$ *a/a* and WT mice at 16, 20 and 24 weeks. **c** Plasma immunoreactive insulin (IRI) levels in *Wfs1*$^{-/-}$ *A*^{y}*/a* (white bars), *Wfs1*$^{+/+}$ *A*^{y}*/a* (hatched bars), *Wfs1*$^{-/-}$ *a/a* (grey bars) and WT (black bars) mice at 12 and 24 weeks of age. Data are presented as the means±SE for n=7–13 mice. ***$p<0.001$

Intraperitoneal glucose tolerance test and ITT were performed at 8 weeks (Fig. 2). *Wfs1*$^{+/+}$ *A*^{y}*/a* mice, as well as *Wfs1*$^{-/-}$ *A*^{y}*/a* mice, were already more insulin-resistant than *Wfs1*$^{+/+}$ *a/a* and *Wfs1*$^{-/-}$ *a/a* mice at this young age (Fig. 2a, d). There was no statistical difference in the ITT curve between *Wfs1*$^{+/+}$ *A*^{y}*/a* and *Wfs1*$^{-/-}$ *A*^{y}*/a* mice. Although glucose tolerance of *Wfs1*$^{+/+}$ *A*^{y}*/a* mice was normal because of compensatory elevated insulin secretion (Fig. 2b, c), this compensation was not found in *Wfs1*$^{-/-}$ *A*^{y}*/a* mice, whose glucose tolerance was impaired (Fig. 2e, f).

A similar, but milder phenotype was observed in the *Wfs1*$^{-/-}$ *a/a* mice with high-fat diet-induced obesity (ESM Fig. 1). The high-fat diet caused obesity with hyperinsulinaemia in WT mice (*Wfs1*$^{+/+}$ *a/a*). However, these mice were normoglycaemic (ESM Fig. 1a). In contrast, a high-fat diet induced hyperglycaemia in *Wfs1*$^{-/-}$ *a/a* mice, although less prominently than in *Wfs1*$^{-/-}$ *A*^{y}*/a* mice (mean non-fasting blood glucose 18.0±2.7 mmol/l, n=6 vs 36.9±2.4 mmol/l, n=14 at 24 weeks of age, $p<0.001$) (ESM Fig. 1b). Non-fasting insulin levels were lower, although not significantly, in high-fat diet-fed *Wfs1*$^{+/+}$ *a/a* than in *Wfs1*$^{+/+}$ *A*^{y}*/a* mice (402.9±87.5 pmol/l, n=9 vs 605.7±114.4, n=7 at age 24 weeks, $p>0.05$) (ESM Fig. 1c).

Acceleration of selective beta cell apoptosis We immunohistochemically investigated the cause of insulin deficiency. In 24-week-old *Wfs1*$^{+/+}$ *A*^{y}*/a* mice, islets were hypertrophic and larger (Fig. 3b, f, j) than in WT (Fig. 3a, e, i) and *Wfs1*$^{-/-}$ *a/a* mice (Fig. 3c, g, k), reflecting responses to the increased insulin demand in *Wfs1*$^{+/+}$ *A*^{y}*/a* mice. In the *Wfs1*$^{-/-}$ *a/a* mice, insulin-positive beta cells were preserved (Fig. 3c, g) and there was no apparent difference from WT controls at this stage, except for a change in islet architecture (aberrant centric migration of alpha cells) (Fig. 3g, [15]). Interestingly and impressively, however, *Wfs1*$^{-/-}$ *A*^{y}*/a* mice had small, irregularly shaped islets, in which insulin-positive beta cells were markedly decreased (Fig. 3d, h).

The results were confirmed by morphometric analysis showing that the insulin-positive area per pancreatic area in *Wfs1*$^{+/+}$ *A*^{y}*/a* mice was increased as compared with that in WT and *Wfs1*$^{-/-}$ *a/a* mice. In *Wfs1*$^{-/-}$ *A*^{y}*/a* mice, the insulin-positive area was markedly reduced (Fig. 4a), as was the pancreatic insulin content (Fig. 4b).

Time courses of beta cell loss in *Wfs1*$^{-/-}$ *A*^{y}*/a* islets are shown in Fig. 3m–o. In *Wfs1*$^{-/-}$ *A*^{y}*/a* mice, insulin-positive beta cells were selectively and severely depleted by

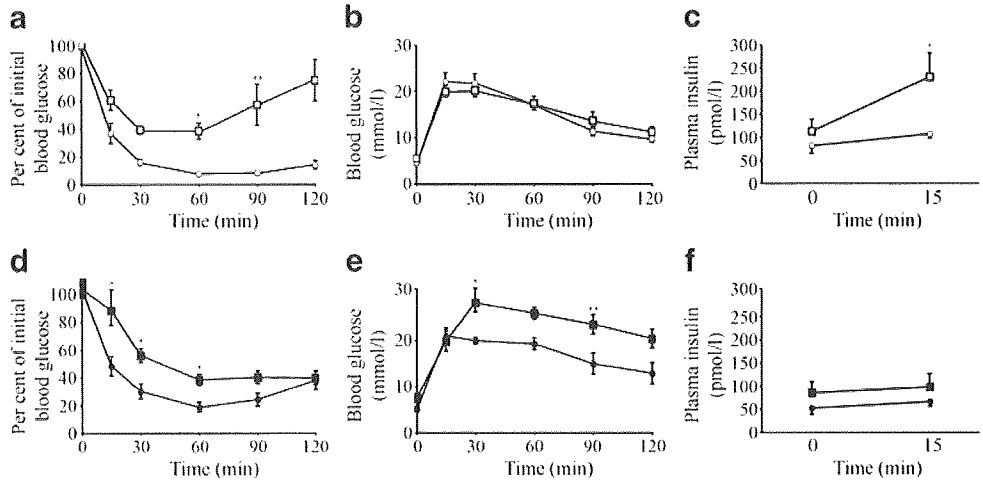

Fig. 2 Insulin tolerance test and ipGTT. ITT (0.75 U/kg) (**a**, **d**) and ipGTT (2 g/kg) (**b**, **c**, **e**, **f**) were performed at 8 weeks of age on *Wfs1*$^{+/+}$*a/a* (WT) (white circles), *Wfs*$^{+/+}$ *A*^{v}*/a* (white squares), *Wfs1*$^{-/-}$*a/a* (black circles) and *Wfs1*$^{-/-}$ *A*^{v}*/a* (black squares). Values are means±SEM, n=3–10 per group (ITT) and n=7–10 per group (ipGTT). *p<0.05, **p<0.01 compared with the corresponding *a/a* mice

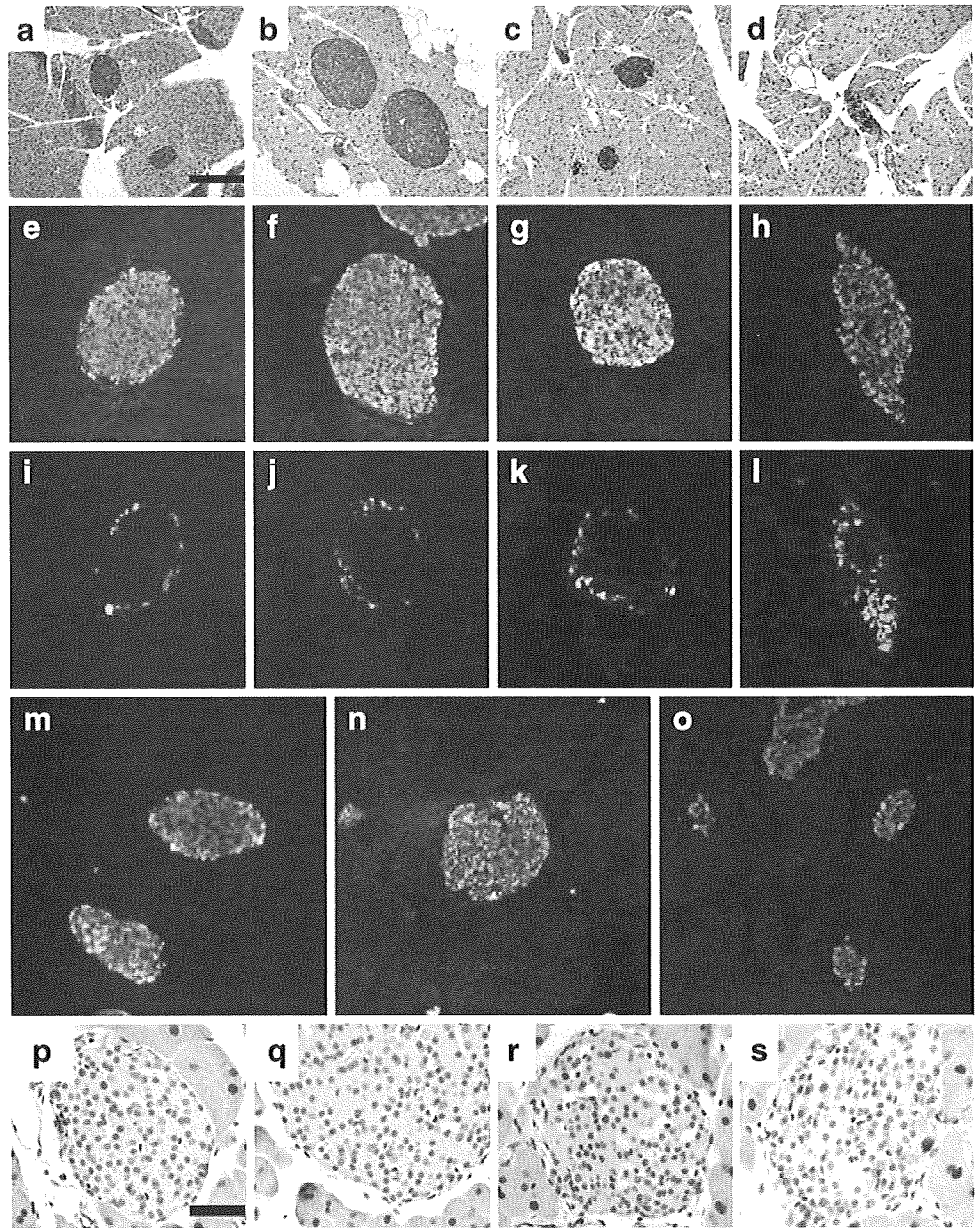

Fig. 3 Selective beta cell loss in islets of *Wfs1*$^{-/-}$ *A*^{v}*/a* mice. **a–l** Pancreatic sections from 24-week-old *Wfs1*$^{+/+}$ *a/a* (WT), *Wfs1*$^{+/+}$ *A*^{v}*/a*, *Wfs1*$^{-/-}$ *a/a* and *Wfs1*$^{-/-}$ *A*^{v}*/a* mice were immunostained for insulin (brown) (**a–d**), scale bar 100 nm. **e–h** Immunofluorescence staining for insulin (green), glucagon (red) and (**i–l**) somatostatin (red). **m–o** Representative time course of beta cell loss in islets from *Wfs1*$^{-/-}$ *A*^{v}*/a* mice. Insulin (green) and glucagon (red) were immunostained. At 8 weeks (**m**), most islets were indistinguishable from those of WT mice. By the 16th week (**n**), normal islet architecture had been destroyed and beta cell numbers were apparently decreased. By week 24 (**o**), few beta cells remained. **p–s** Immunohistochemistry results for pro-apoptotic active caspase-3 in pancreatic sections from WT (**p**), *Wfs1*$^{+/+}$ *A*^{v}*/a* (**q**), *Wfs1*$^{-/-}$ *a/a* (**r**) and *Wfs1*$^{-/-}$ *A*^{v}*/a* mice (**s**). Activated caspase-3 staining was performed at age 16 weeks. Positive cells were found in *Wfs1*$^{-/-}$ *A*^{v}*/a* islets (**s**), but not in islets from other mice. Scale bar, 50 nm

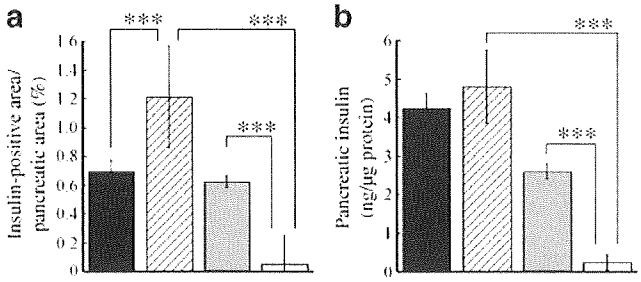

Fig. 4 Insulin-positive areas and insulin content of pancreases. **a** Ratios of total insulin-positive area to the entire pancreatic area were estimated for *Wfs1*$^{+/+}$ *a/a* (WT, black bars), *Wfs1*$^{+/+}$ *A*^{y}*/a* (hatched bars), *Wfs1*$^{-/-}$ *a/a* (grey bars) and the *Wfs1*$^{-/-}$ *A*^{y}*/a* (white bars) mice at age 24 weeks. At least five sections from each mouse were prepared and examined. Data are means±SE from four animals for each group. ***$p<0.001$. **b** Insulin contents extracted from whole pancreases of WT, *Wfs1*$^{+/+}$ *A*^{y}*/a*, *Wfs1*$^{-/-}$ *a/a* and *Wfs1*$^{-/-}$ *A*^{y}*/a* mice (key as above) at age 24 weeks (means±SE, $n=7$). ***$p<0.001$

24 weeks of age, whereas glucagon-positive alpha cells and somatostatin-positive delta cells were preserved (Fig. 3h, l). This selective beta cell loss was due to apoptotic cell death as indicated by caspase-3 activation in islets of 16-week-old mice (Fig. 3p–s).

Ultrastructural analysis We performed ultrastructural analyses of pancreatic beta cells from 12-week-old mice using electron microscopy. The beta cells were distinguished from alpha and delta cells by the appearance of their secretory granules. The beta cell granules had a white halo, not evident in alpha and delta cell granules.

In *A*^{y}*/a* mice pancreatic beta cells, rough ER was well developed and structurally indistinguishable from that of WT mice (Fig. 5a, b, e, f). In *Wfs1*$^{-/-}$ *a/a* mice, ER was dilated and beta cell secretory granules were electron-lucent in some pancreatic beta cells (Fig. 5c, g). In contrast, in *Wfs1*$^{-/-}$ *A*^{y}*/a* mice, ER was severely dilated in almost all pancreatic beta cells and secretory granules were reduced in size and electron density (Fig. 5d, h). In addition, mitochondrial swelling was observed in these beta cells. ER abnormality appears to be a common finding in rodent models of ER stress-related beta cell failure [26, 29, 30]. Riggs et al. reported similar findings in their beta cell-specific *Wfs1* knockout mouse [22]. Changes were milder in their mice than in our *Wfs1*$^{-/-}$ *A*^{y}*/a* mice and no mitochondrial abnormalities were mentioned. The difference may represent different stages of the same process.

Unfolded protein response in pancreatic islets of obese and Wfs1$^{-/-}$ *mice* Our group and others have shown that *Wfs1*$^{-/-}$ beta cells are susceptible to ER stress and that WFS1 deficiency itself evokes the UPR [15, 20, 22]. If insulin resistance induces ER stress in pancreatic beta cells via increased demand for insulin biosynthesis and secretion, beta cell death would presumably be accelerated in *Wfs1*$^{-/-}$ mice that become insulin-resistant. To examine this possibility, we first analysed WFS1 protein levels and the UPR in beta cells under insulin-resistant conditions. Western blot analysis at 12 weeks, when some mice were already hyperglycaemic, but more than half remained essentially normoglycaemic (Fig. 1b), revealed WFS1 protein levels to be increased in obese *Wfs1*$^{+/+}$ *A*^{y}*/a* murine islets as compared with those in *Wfs1*$^{+/+}$ a/a (WT) mice (Fig. 6a). Levels of ER chaperones 94 kDa glucose-regulated protein (GRP94) and 78 kDa glucose-regulated protein (GRP78) were also apparently increased in *Wfs1*$^{+/+}$ *A*^{y}*/a* and *Wfs1*$^{-/-}$ *a/a* mice as compared

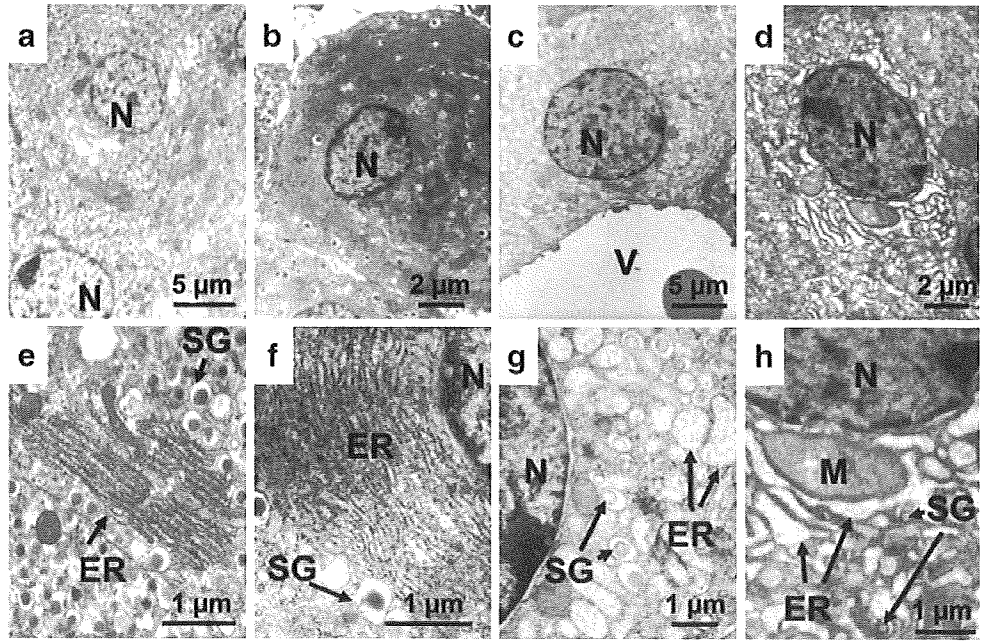

Fig. 5 Electron micrograph of pancreatic beta cells. Ultrastructural analysis using electron microscopy was performed on islets from *Wfs1*$^{+/+}$ *a/a* (WT) (**a**, **e**), *Wfs1*$^{+/+}$ *A*^{y}*/a* (**b**, **f**), *Wfs1*$^{-/-}$ *a/a* (**c**, **g**) and *Wfs1*$^{-/-}$ *A*^{y}*/a* mice (**d**, **h**) at age 12 weeks. Magnification was as shown, i.e. lower (**a–d**) and higher (**e–h**). M, mitochondrion; N, nucleus; SG, secretory granule; V, blood vessel

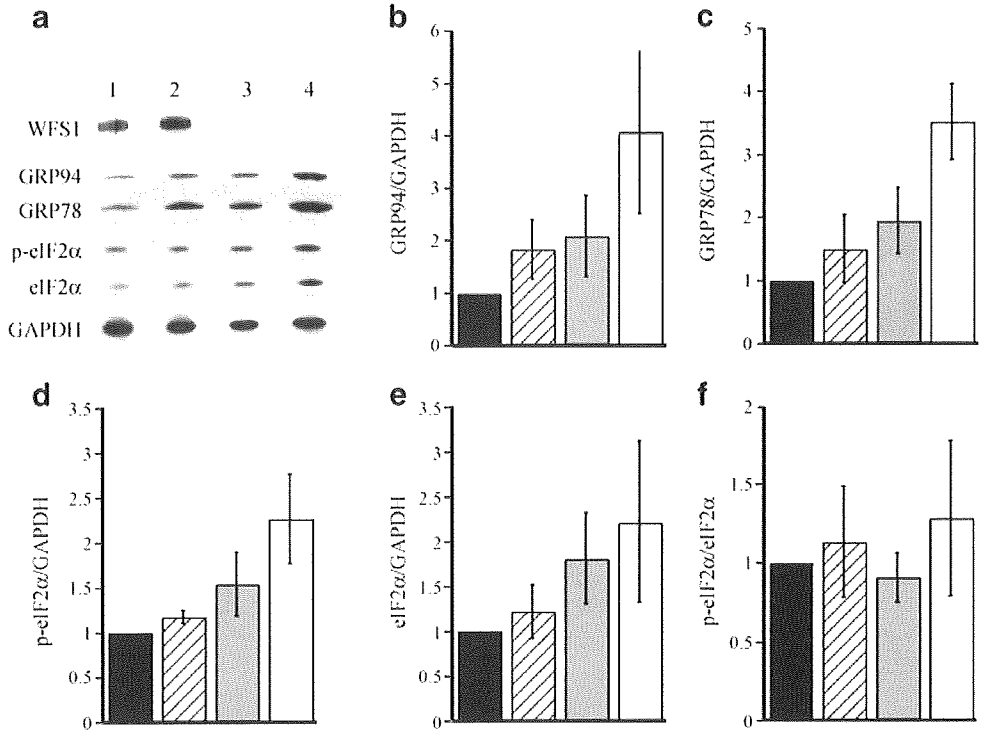

Fig. 6 Unfolded protein responses of pancreatic islets. **a** Isolated murine islets were subjected to SDS/PAGE and blotted using antibodies directed against WFS1 (N-terminus), C-terminal lys-asp-glu-leu (GRP94, GRP78), eIF2α, phosphorylated eIF2α (p-eIF2α) and glyceraldehyde 3-phosphate dehydrogenase (GAPDH). Lane 1, *Wfs1*$^{+/+}$ *a/a* (WT); lane 2, *Wfs*$^{+/+}$ *A*^{v}*/a;* lane 3, *Wfs*$^{-/-}$ *a/a*; lane 4, *Wfs*$^{-/-}$ *A*^{v}*/a*. The blot is representative of experiments repeated three times. **b–f** Summary of respective protein/GAPDH levels from three independent experiments. Data (means±SE) are expressed relative to those of the *Wfs1*$^{+/+}$ *a/a* (WT) islet preparation. Although the differences did not reach statistical significance, the UPR tended to be enhanced in *Wfs*$^{+/+}$ *A*^{v}*/a* (hatched bars) and *Wfs*$^{-/-}$ *a/a* (grey bars) mice as compared with the WT (*Wfs*$^{+/+}$ *a/a)* (black bars) mice, and appeared to be further enhanced in *Wfs*$^{-/-}$ *A*^{v}*/a* (white bars) mice. Experiments were performed using 12-week-old mice

with WT mice (Fig. 6a–c). Therefore, ER stress had been triggered in *A*^{v}*/a* and *Wfs1*$^{-/-}$ mice. In *Wfs1*$^{-/-}$ *A*^{v}*/a* mice, levels of these ER chaperones appeared to be further increased (Fig. 6a–c). Phosphorylation of the translation initiation factor-2, subunit α (eIF2α) attenuates protein translation under ER stress conditions. Similar changes were observed in total eIF2α protein and phosphorylated eIF2α amounts in the islets of *Wfs1*$^{+/+}$ *A*^{v}*/a*, *Wfs1*$^{-/-}$ *a/a* and *Wfs1*$^{-/-}$ *A*^{v}*/a* mice (Fig. 6a, d–f). We also measured *Grp78* (also known as *Hspa5*), *Grp94* (also known as *Hsp90b1*) and spliced *Xbp1* mRNA expression in 8-week-old mice islets. A similar trend was observed, although changes were less prominent at this age (ESM Fig. 2). These data suggest that *A*^{v}*/a* murine islets are exposed to ER stress and that increased ER stress is among the likely causes of rapid and prominent beta cell apoptosis in *Wfs1*$^{-/-}$ *A*^{v}*/a* murine islets.

Pioglitazone prevented beta cell loss and diabetes in Wfs1$^{-/-}$ *A*^{v}*/a mice* Our observations suggest that beta cell overload markedly accelerates beta cell death and diabetes development in *Wfs1*$^{-/-}$ *a/a* mice. Therefore, we attempted to reduce this beta cell overload, which is likely to be due to obesity-associated insulin resistance, with pioglitazone treatment. Mice were allowed free access to normal chow containing 0.01% pioglitazone immediately after weaning (4 weeks of age). The average dose of pioglitazone was estimated to be 15 mg kg^{-1} day^{-1}.

Pioglitazone ameliorated insulin resistance as assessed by the non-fasting insulin levels in *Wfs1*$^{+/+}$ *A*^{v}*/a* mice (mean non-fasting insulin without pioglitazone 513.5± 49.9 pmol/l, n=13 vs with pioglitazone 326.9±61.0 pmol/l, n=7, p<0.05) at 12 weeks of age. Serum triacylglycerol levels were also markedly improved (Fig. 7). The *Wfs1*$^{-/-}$ *A*^{v}*/a* mice gained more weight with pioglitazone treatment. As early as 7 weeks of age, *Wfs1*$^{-/-}$ *A*^{v}*/a* mice treated with pioglitazone were heavier (28.7±0.7 g, n=11) than *Wfs1*$^{+/+}$ *A*^{v}*/a* (25.5±0.7 g, n=15, p<0.01) and *Wfs1*$^{-/-}$ *A*^{v}*/a* (26.0± 0.4 g, n=20, p<0.01) mice fed normal chow (Fig. 8a). Despite the increased body weight, pioglitazone prevented diabetes development. Average non-fasted blood glucose levels were significantly lower in pioglitazone-treated *Wfs1*$^{-/-}$ *A*^{v}*/a* mice than in untreated *Wfs1*$^{-/-}$ *A*^{v}*/a* mice (12.9±0.9 vs 20.5±1.9 mmol/l, p<0.002) at 16 weeks (Fig. 8b). Histological analyses revealed pancreatic beta cells to be very well preserved in pioglitazone-treated *Wfs1*$^{-/-}$ *A*^{v}*/a* mice (Fig. 8c–f).

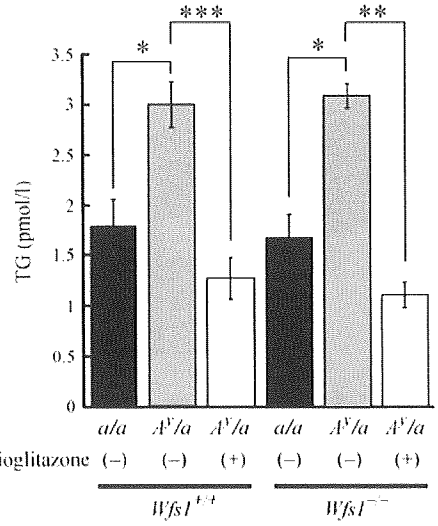

Fig. 7 Serum triacylglycerol (TG) levels with/without pioglitazone. Serum triacylglycerol levels were measured in 12-week-old mice. After weaning (4 weeks of age), the mice were fed standard mouse chow with/without 0.01% pioglitazone. Values are means±SE from three to five mice. *$p<0.05$, **$p<0.01$, ***$p<0.001$

Pioglitazone did not suppress the UPR To investigate whether pioglitazone treatment reduces ER stress in pancreatic beta cells, we examined UPR activation by Western blot analysis using isolated murine islets. Interestingly and unexpectedly, pioglitazone did not reduce either ER chaperones or eIF2α levels/phosphorylation in *Wfs1*$^{-/-}$ *a/a* and *Wfs1*$^{-/-}$ *A*^{y}*/a* mice (Fig. 9a, ESM Fig. 3). Similar results were obtained for spliced *Xbp1*, *Grp78*, *Grp94* and *Chop* (also known as *Ddit3*) mRNA expression in 8-week-old mice islets (ESM Fig. 2).

Electron microscopic examination revealed markedly improved ER appearance in *Wfs1*$^{-/-}$ *A*^{y}*/a* pancreatic beta cells after pioglitazone treatment (Fig. 9b–e, see also Fig. 5). Without the treatment, almost all beta cells had markedly distended ER (Fig. 9b, c). However, after the treatment, the ER distension was markedly reduced and some beta cells appeared to be normal (Fig. 9d, e), although heterogeneity was observed among the cells.

Discussion

Here we demonstrated that *Wfs1*$^{-/-}$ *A*^{y}*/a* mice on a C57BL/6J background develop early-onset insulin-deficient diabetes mellitus as early as 6 weeks of age and that most are overtly diabetic by the 16th week, whereas neither *Wfs1*-deficient *Wfs1*$^{-/-}$ *a/a* nor obese agouti yellow (*Wfs1*$^{+/+}$ *A*^{y}*/a*) mice had developed overt diabetes by the 24th week. In *Wfs1*$^{-/-}$ *A*^{y}*/a* murine islets, beta cell mass was dramatically decreased due to increased beta cell apoptosis. WFS1 protein clearly plays a pivotal role in beta cell survival.

Our previous study had demonstrated that approximately half of *Wfs1*$^{-/-}$ mice develop diabetes when they have the hybrid genetic background of C57BL/6J and 129Sv, while. unexpectedly with the C57BL/6J background, there is no apparent increase in blood glucose levels even at 36 weeks [15]. Because beta cells of *Wfs1*$^{-/-}$ mice were also shown to be susceptible to ER stress in ex-vivo experiments and cultured cells [15, 21], we sought to test this in the in vivo model.

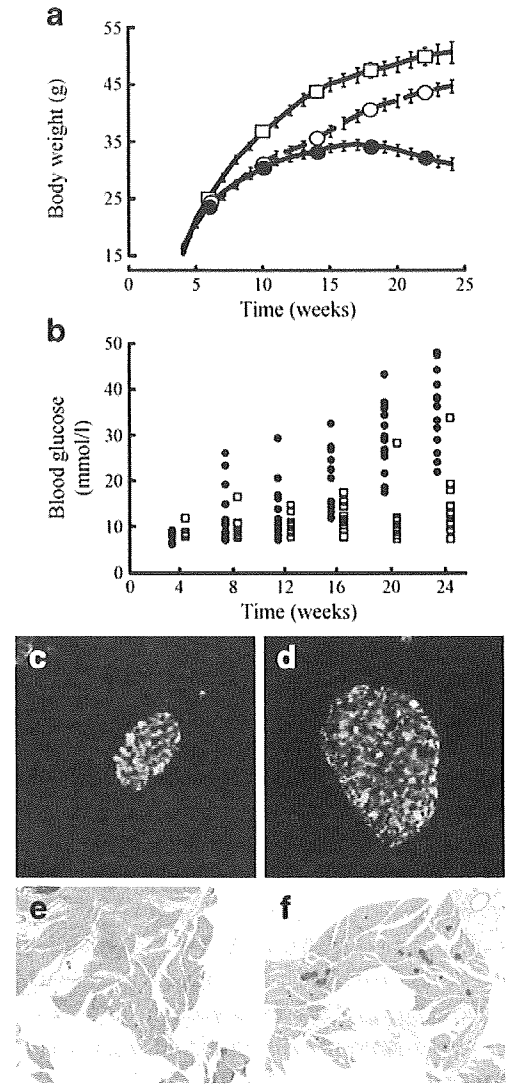

Fig. 8 Pioglitazone prevents diabetes and beta cell loss. The standard mouse chow with 0.01% pioglitazone was started at 4 and continued until 24 weeks of age in *Wfs1*$^{-/-}$ *A*^{y}*/a* mice. **a** Graph showing body weight changes (means±SE, $n=11$–20) and (**b**) non-fasted blood glucose levels ($n=11$–16). Black circles, *Wfs1*$^{-/-}$ *A*^{y}*/a* mice without treatment; squares, *Wfs1*$^{-/-}$ *A*^{y}*/a* mice with pioglitazone treatment; white circles, control *Wfs1*$^{+/+}$ *A*^{y}*/a* mice. **c** Insulin (green) and glucagon (red) were stained in pancreatic sections from *Wfs1*$^{-/-}$ *A*^{y}*/a* mice and (**d**) from pioglitazone-treated *Wfs1*$^{-/-}$ *A*^{y}*/a* mice at 24 weeks of age. **e** Insulin (brown) was stained in pancreatic sections from *Wfs1*$^{-/-}$ *A*^{y}*/a* mice and (**f**) from pioglitazone-treated *Wfs1*$^{-/-}$ *A*^{y}*/a* mice at 24 weeks of age

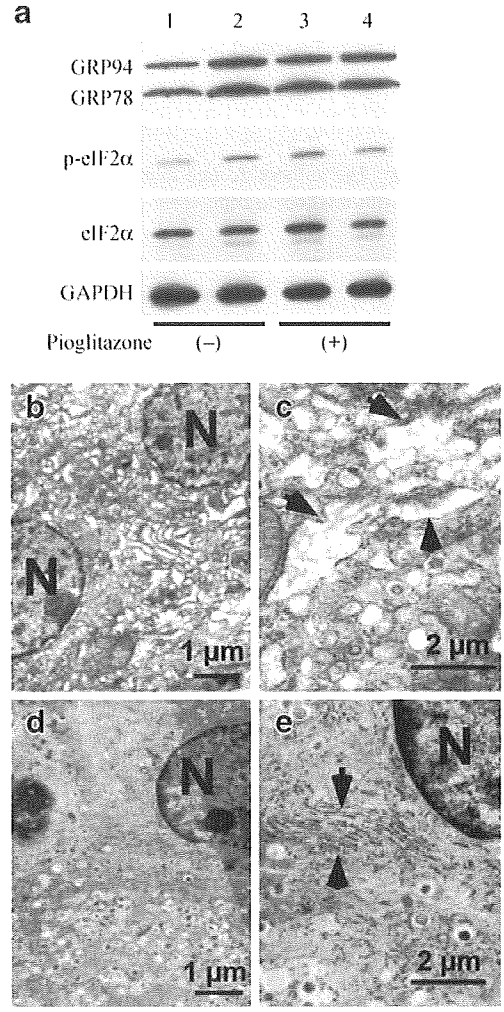

Fig. 9 Unfolded protein responses and ultrastructural changes in beta cells after pioglitazone treatment. **a** *Wfs1*$^{-/-}$ *a/a* (lanes 1, 3) and *Wfs1*$^{-/-}$ *A*^{y}*/a* (lanes 2, 4) mice were fed standard mouse chow with/without 0.01% pioglitazone after weaning (4 weeks of age). Isolated murine islets at 12 weeks of age were subjected to SDS/PAGE and blotted using antibodies directed against WFS1 (N-terminus), C-terminal lys-asp-glu-leu (GRP94, GRP78), eIF2α, phosphorylated eIF2α (p-eIF2α) and glyceraldehyde 3-phosphate dehydrogenase (GAPDH). The blot is representative of three independent experiments. Densitometric quantification of these results is presented in ESM Fig. 3). Electron micrographs of islets from *Wfs1*$^{-/-}$ *A*^{y}*/a* mice (12-week-old) without (**b**, **c**) or with (**d**, **e**) pioglitazone treatment. Arrows, ER; N, nucleus

The *A*^{y}*/a* mouse is a genetic model of mild obesity/insulin resistance with compensatory beta cell hyperplasia [31] (Figs 1 and 3). Increased demand for insulin biosynthesis and secretion has been thought to cause ER stress in pancreatic beta cells, and here, in fact, we demonstrated, in *A*^{y}*/a* murine islets, that ER chaperone expression was apparently increased at 12 weeks of age (Fig. 6). Similar results have been demonstrated in another insulin-resistant mouse model [7]. In addition, WFS1 protein levels were also increased (Fig. 6a). Our group and others have shown WFS1 protein levels to be upregulated by ER stress [19, 20, 35]. These data suggest that increased insulin demand under insulin-resistant conditions produces chronic ER stress in beta cells. In addition, NEFA, which are elevated in these insulin-resistant models, may also contribute to the activation of UPR [32]. In this regard, Lipson et al. recently demonstrated that hyperglycaemia activates inositol-requiring protein-1 (IRE1)α, an ER-resident transmembrane protein kinase regulating UPR in beta cells. Although IRE1α activation by transient hyperglycaemia is beneficial to beta cells, chronically sustained hyperglycaemia causes ER stress and suppresses insulin gene expression [36]. Glucose regulation of the UPR has also been reported [37].

Dramatically decreased beta cell numbers in *Wfs1*$^{-/-}$ *A*^{y}*/a* mice suggest that increased insulin demand triggers pancreatic beta cell apoptosis in *Wfs1*-deficient mice. ER stress induces WFS1 protein production and lack of this protein itself enhances the UPR [15, 19–21]. This was true in our mice (Fig. 6), with the UPR apparently further enhanced in mildly obese *Wfs1*$^{-/-}$ *A*^{y}*/a* mice. These data support the hypothesis that beta cell loss in Wolfram syndrome is, at least partly, caused by increased ER stress in beta cells. Although the precise function of ER-resident WFS1 protein remains unknown, our overall results suggest that this protein is likely to protect beta cells from ER stress-induced apoptosis and that Wolfram syndrome is an ER stress-related disease.

In patients with type 2 diabetes, very gradual, but progressive beta cell loss is caused by many factors, both genetic and acquired. One well-established mechanism of acquired beta cell loss is oxidative stress, which appears to be a major mediator of glucotoxicity [38]. We observed 4-hydroxy-2-nonenal-modified protein, an oxidative stress marker, in *Wfs1*$^{-/-}$ *A*^{y}*/a* murine islets at age 16 weeks (data not shown), suggesting that oxidative stress is also involved in beta cell apoptosis. Oxidative stress is likely to have been secondary to chronic hyperglycaemia because most *Wfs1*$^{-/-}$ *A*^{y}*/a* mice had developed hyperglycaemia by this age (Fig. 1b). In *Wfs1*$^{-/-}$ *A*^{y}*/a* mice, the vicious cycle associated with ER stress and oxidative stress probably exacerbates beta cell apoptosis. In this regard, it is again worth emphasising that insulin resistance induces ER stress in pancreatic beta cells [7]. Currently, we do not know the full extent of ER stress involvement in beta cell failure in human type 2 diabetes. However, it is possible that this vicious cycle associated with ER stress and oxidative stress plays an important role in beta cell deterioration [39].

Pioglitazone treatment almost completely prevented the development of diabetes and beta cell loss in *Wfs1*$^{-/-}$ *A*^{y}*/a* mice. One simple explanation is that insulin resistance was ameliorated by pioglitazone treatment, reducing ER stress in pancreatic beta cells and preventing beta cell death.

However, the mechanism may not be so simple. Unexpectedly, the UPR, represented by ER chaperone expression, was not significantly reduced (Fig. 9a, ESM Figs 2 and 3) to the extent that we expected from the remarkable level of diabetes prevention. Because the UPR is a protective response against ER stress, an apoptotic pathway may have been preferentially suppressed under these conditions. Several pathways are reportedly involved in ER stress-induced apoptosis, including the C/EBP-homologous protein (CHOP), the IRE1–TNF receptor-associated factor 2 (TRAF2)–apoptosis signal-regulating kinase 1 (ASK1), and the caspase 12 pathways [40]. The precise mechanism whereby pioglitazone prevented apoptosis in beta cells awaits determination. The beta cell protection exerted by thiazolidinediones including pioglitazone has been demonstrated in other rodent models [41, 42] and also in humans [43]. Although the precise mechanisms are not fully understood, one possibility is an indirect action through improvements in systemic glucose and lipid metabolism. Another mechanism involves direct actions on pancreatic beta cells [44]. Recent reports have demonstrated that thiazolidinediones directly improve beta cell function [45], ameliorate lipotoxicity [46] and prevent beta cell apoptosis [47, 48]. In *Wfs1*$^{-/-}$ *A*^{y}*/a* mice, direct protective effects, as well as indirect effects, are likely to be exerted. Elucidation of the mechanism whereby pioglitazone directly protects beta cells against apoptosis in *Wfs1*$^{-/-}$ *A*^{y}*/a* mice would provide insights into the mechanism of beta cell death in patients with Wolfram syndrome, as well as the function of WFS1 protein in beta cells.

This is one of a few good models showing that one genetic defect predisposes beta cells to profound failure upon ER stress induced by systemic insulin resistance [30, 49]. Our findings are important for the understanding of the molecular pathophysiology of Wolfram syndrome. In addition, a common process may be involved in conventional type 2 diabetes patients, whose beta cells decrease very slowly but progressively. In this context, a recent report has confirmed that common variants in the *WFS1* gene confer risk of type 2 diabetes [50]. Therefore knowledge from this model would help us to understand the mechanisms of, and to develop a way of preventing beta cell loss in patients with conventional type 2 diabetes mellitus.

Acknowledgements We thank M. Nishimura (Nagoya University Graduate School of Medicine) for kindly providing C57BL/6J*HamSlc*-A^{y} mice. This study was supported in part by Grants-in-Aid for Scientific Research (grant no16390096, 18390103 and 20390093 to Y. Tanizawa) from the Ministry of Education, Culture, Sports, Science and Technology of Japan, grant no. 16790510 (to K. Ueda) from the Japan Society for the Promotion of Science, grant H16-genome-003 (to Y. Oka and Y. Tanizawa) from the Ministry of Health, Labour and Welfare of Japan, and a grant from the Takeda Science Foundation (to Y. Tanizawa).

Duality of interest The authors declare that there is no duality of interest associated with this manuscript.

References

1. Rhodes CJ (2005) Type 2 diabetes—a matter of beta-cell life and death? Science 307:380–384
2. Butler AE, Janson J, Bonner-Weir S, Ritzel R, Rizza RA, Butler PC (2003) Beta-cell deficit and increased beta-cell apoptosis in humans with type 2 diabetes. Diabetes 52:102–110
3. Sakuraba H, Mizukami H, Yagihashi N, Wada R, Hanyu C, Yagihashi S (2002) Reduced beta-cell mass and expression of oxidative stress-related DNA damage in the islet of Japanese Type II diabetic patients. Diabetologia 45:85–96
4. Poitout V, Robertson RP (2008) Glucolipotoxicity: fuel excess and beta-cell dysfunction. Endocr Rev 29:351–366
5. Eizirik DL, Cardozo AK, Cnop M (2008) The role for endoplasmic reticulum stress in diabetes mellitus. Endocr Rev 29:42–61
6. Marchetti P, Bugliani M, Lupi R et al (2007) The endoplasmic reticulum in pancreatic beta cells of type 2 diabetes patients. Diabetologia 50:2486–2494
7. Laybutt DR, Preston AM, Akerfeldt MC et al (2007) Endoplasmic reticulum stress contributes to beta cell apoptosis in type 2 diabetes. Diabetologia 50:752–763
8. Barrett TG, Bundey SE (1997) Wolfram (DIDMOAD) syndrome. J Med Genet 34:838–841
9. Barrett TG, Bundey SE, Macleod AF (1995) Neurodegeneration and diabetes: UK nationwide study of Wolfram (DIDMOAD) syndrome. Lancet 346:1458–1463
10. Karasik A, O'Hara C, Srikanta S et al (1989) Genetically programmed selective islet beta-cell loss in diabetic subjects with Wolfram's syndrome. Diabetes Care 12:135–138
11. Inoue H, Tanizawa Y, Wasson J et al (1998) A gene encoding a transmembrane protein is mutated in patients with diabetes mellitus and optic atrophy (Wolfram syndrome). Nat Genet 20:143–148
12. Strom TM, Hortnagel K, Hofmann S et al (1998) Diabetes insipidus, diabetes mellitus, optic atrophy and deafness (DIDMOAD) caused by mutations in a novel gene (wolframin) coding for a predicted transmembrane protein. Hum Mol Genet 7:2021–2028
13. Takeda K, Inoue H, Tanizawa Y et al (2001) WFS1 (Wolfram syndrome 1) gene product: predominant subcellular localization to endoplasmic reticulum in cultured cells and neuronal expression in rat brain. Hum Mol Genet 10:477–484
14. Hofmann S, Philbrook C, Gerbitz KD, Bauer MF (2003) Wolfram syndrome: structural and functional analyses of mutant and wild-type wolframin, the WFS1 gene product. Hum Mol *Genet* 12:2003–2012
15. Ishihara H, Takeda S, Tamura A et al (2004) Disruption of the WFS1 gene in mice causes progressive beta-cell loss and impaired stimulus-secretion coupling in insulin secretion. Hum Mol Genet 13:1159–1170
16. Osman AA, Saito M, Makepeace C, Permutt MA, Schlesinger P, Mueckler M (2003) Wolframin expression induces novel ion channel activity in endoplasmic reticulum membranes and increases intracellular calcium. J Biol Chem 278:52755–52762

17. Takei D, Ishihara H, Yamaguchi S et al (2006) WFS1 protein modulates the free Ca^{2+} concentration in the endoplasmic reticulum. FEBS Lett 580:5635–5640
18. Zatyka M, Ricketts C, da Silva Xavier G et al (2008) Sodium-potassium ATPase 1 subunit is a molecular partner of Wolframin, an endoplasmic reticulum protein involved in ER stress. Hum Mol Genet 17:190–200
19. Fonseca SG, Fukuma M, Lipson KL et al (2005) WFS1 is a novel component of the unfolded protein response and maintains homeostasis of the endoplasmic reticulum in pancreatic beta-cells. J Biol Chem 280:39609–39615
20. Ueda K, Kawano J, Takeda K et al (2005) Endoplasmic reticulum stress induces Wfs1 gene expression in pancreatic beta-cells via transcriptional activation. Eur J Endocrinol 153:167–176
21. Yamada T, Ishihara H, Tamura A et al (2006) WFS1-deficiency increases endoplasmic reticulum stress, impairs cell cycle progression and triggers the apoptotic pathway specifically in pancreatic beta-cells. Hum Mol Genet 15:1600–1609
22. Riggs AC, Bernal-Mizrachi E, Ohsugi M et al (2005) Mice conditionally lacking the Wolfram gene in pancreatic islet beta cells exhibit diabetes as a result of enhanced endoplasmic reticulum stress and apoptosis. Diabetologia 48:2313–2321
23. Schroder M, Kaufman RJ (2005) The mammalian unfolded protein response. Annu Rev Biochem 74:739–789
24. Ron D, Walter P (2007) Signal integration in the endoplasmic reticulum unfolded protein response. Nat Rev Mol Cell Biol 8:519–529
25. Scheuner D, Kaufman RJ (2008) The unfolded protein response: a pathway that links insulin demand with beta-cell failure and diabetes. Endocr Rev 29:317–333
26. Harding HP, Zeng H, Zhang Y et al (2001) Diabetes mellitus and exocrine pancreatic dysfunction in $perk^{-/-}$ mice reveals a role for translational control in secretory cell survival. Mol Cell 7:1153–1163
27. Delepine M, Nicolino M, Barrett T, Golamaully M, Lathrop GM, Julier C (2000) *EIF2AK3*, encoding translation initiation factor 2-alpha kinase 3, is mutated in patients with Wolcott-Rallison syndrome. Nat Genet 25:406–409
28. Scheuner D, Song B, McEwen E et al (2001) Translational control is required for the unfolded protein response and in vivo glucose homeostasis. Mol Cell 7:1165–1176
29. Wang J, Takeuchi T, Tanaka S et al (1999) A mutation in the insulin 2 gene induces diabetes with severe pancreatic beta-cell dysfunction in the Mody mouse. J Clin Invest 103:27–37
30. Scheuner D, Vander MD, Song B et al (2005) Control of mRNA translation preserves endoplasmic reticulum function in beta cells and maintains glucose homeostasis. Nat Med 11:757–764
31. Wolff GL, Roberts DW, Mountjoy KG (1999) Physiological consequences of ectopic agouti gene expression: the yellow obese mouse syndrome. Physiol Genomics 11:151–163
32. Cunha DA, Hekerman P, Ladrière L et al (2008) Initiation and execution of lipotoxic ER stress in pancreatic beta-cells. J Cell Sci 121:2308–2318
33. Usui S, Hara Y, Hosaki S, Okazaki M (2002) A new on-line dual enzymatic method for simultaneous quantification of cholesterol and triglycerides in lipoproteins by HPLC. J Lipid Res 43:805–814
34. Oka Y, Asano T, Shibasaki Y, Kasuga M, Kanazawa Y, Takaku F (1988) Studies with antipeptide antibody suggest the presence of at least two types of glucose transporter in rat brain and adipocyte. J Biol Chem 263:13432–13439
35. Yamaguchi S, Ishihara H, Tamura A (2004) Endoplasmic reticulum stress and N-glycosylation modulate expression of WFS1 protein. Biochem Biophys Res Commun 325:250–256
36. Lipson KL, Fonseca SG, Ishigaki S et al (2006) Regulation of insulin biosynthesis in pancreatic beta cells by an endoplasmic reticulum-resident protein kinase IRE1. Cell Metab 4:245–254
37. Elouil H, Bensellam M, Guiot Y et al (2007) Acute nutrient regulation of the unfolded protein response and integrated stress response in cultured rat pancreatic islets. Diabetologia 50:1442–1452
38. Robertson RP, Harmon JS (2006) Diabetes, glucose toxicity, and oxidative stress: a case of double jeopardy for the pancreatic islet beta cell. Free Radic Biol Med 41:177–184
39. Malhotra JD, Kaufman RJ (2007) Endoplasmic reticulum stress and oxidative stress: a vicious cycle or a double-edged sword? Antioxid Redox Signal 9:2277–2293
40. Yoshida H (2007) ER stress and diseases. FEBS J 274:630–658
41. Ishida H, Takizawa M, Ozawa S (2004) Pioglitazone improves insulin secretory capacity and prevents the loss of beta-cell mass in obese diabetic db/db mice: possible protection of beta cells from oxidative stress. Metabolism 53:488–494
42. Diani AR, Sawada G, Wyse B, Murray FT, Khan M (2004) Pioglitazone preserves pancreatic islet structure and insulin secretory function in three murine models of type 2 diabetes. Am J Physiol Endocrinol Metab 286:116–122
43. Dormandy JA, Charbonnel B, Eckland DJ et al (2005) Secondary prevention of macrovascular events in patients with type 2 diabetes in the PROactive Study (PROspective pioglitAzone Clinical Trial In macroVascular Events): a randomised controlled trial. Lancet 366:1279–1289
44. Rosen ED, Kulkarni RN, Sarraf P et al (2003) Targeted elimination of peroxisome proliferator-activated receptor gamma in beta cells leads to abnormalities in islet mass without compromising glucose homeostasis. Mol Cell Biol 23:7222–7229
45. Kim HI, Ahn YH (2004) Role of peroxisome proliferator-activated receptor-gamma in the glucose-sensing apparatus of liver and beta-cells. Diabetes 53(Suppl 1):S60–S65
46. Saitoh Y, Chun-ping C, Noma K et al (2008) Pioglitazone attenuates fatty acid-induced oxidative stress and apoptosis in pancreatic beta-cells. Diabetes Obes Metab 10:564–573
47. Lin CY, Gurlo T, Haataja L, Hsueh WA, Butler PC (2005) Activation of peroxisome proliferator-activated receptor-gamma by rosiglitazone protects human islet cells against human islet amyloid polypeptide toxicity by a phosphatidylinositol 3′-kinase-dependent pathway. J Clin Endocrinol Metab 90:6678–6686
48. Zeender E, Maedler K, Bosco D et al (2004) Pioglitazone and sodium salicylate protect human beta-cells against apoptosis and impaired function induced by glucose and interleukin-1beta. J Clin Endocrinol Metab 89:5059–5066
49. Huang C, Lin C, Haataja L et al (2007) High expression rates of human islet amyloid polypeptide induce endoplasmic reticulum stress-mediated beta-cell apoptosis, a characteristic of humans with type 2 but not type 1 diabetes. Diabetes 56:2016–2027
50. Sandhu MS, Weedon MN, Fawcett KA et al (2007) Common variants in *WFS1* confer risk of type 2 diabetes. Nat Genet 39:951–953

Atherosclerosis 206 (2009) 168–172

Contents lists available at ScienceDirect

Atherosclerosis

journal homepage: www.elsevier.com/locate/atherosclerosis

Carotid arterial elasticity is a sensitive atherosclerosis value reflecting visceral fat accumulation in obese subjects

Ai Tokita[a], Yasushi Ishigaki[a], Hisashi Okimoto[a], Hideyuki Hasegawa[c], Yoshiro Koiwa[d], Makoto Kato[e], Hisamitsu Ishihara[a], Yoshinori Hinokio[a], Hideki Katagiri[b], Hiroshi Kanai[c], Yoshitomo Oka[a,*]

[a] Division of Molecular Metabolism and Diabetes, Tohoku University Graduate School of Medicine, 2-1 Seiryo-machi, Aoba-ku, Sendai 980-8575, Japan
[b] Division of Advanced Therapeutics for Metabolic Diseases, Tohoku University Graduate School of Medicine, Japan
[c] Department of Electrical Engineering, Tohoku University Graduate School of Engineering, Tohoku University, Sendai, Japan
[d] Oizumi Memorial Hospital, Shiroishi, Japan
[e] Panasonic Shikoku Electronics Co., Ltd., Yokohama, Japan

ARTICLE INFO

Article history:
Received 30 August 2008
Received in revised form 29 January 2009
Accepted 30 January 2009
Available online 20 February 2009

Keywords:
Elasticity
Obesity
Ultrasound
Visceral adiposity
Early stage atherosclerosis

ABSTRACT

Background: We previously reported the arterial elasticity value we measured to reflect the characteristic features of vessel walls, and to possibly be useful for detecting early stage atherosclerosis in type 2 diabetes. Obesity, especially visceral adiposity, is well known to play a crucial role in the development of metabolic disorders and atherosclerosis. To assess whether arterial elasticity value reflects the effect of obesity on atherosclerosis, we examined the associations of obesity characteristics with atherosclerosis values including arterial elasticity, carotid intima–media thickness (IMT) and pulse wave velocity (PWV).
Methods: Three atherosclerosis values were measured in 78 obese subjects (body mass index ≥30). We investigated the associations of atherosclerosis values with obesity-related parameters including abdominal fat accumulation determined by computed tomography.
Results: Arterial elasticity values were positively related to established atherosclerosis values, carotid IMT and PWV, in obese subjects. Age, systolic blood pressure and hypertension also correlated with these atherosclerosis values. Single regression analysis showed all three atherosclerosis values to correlate significantly with visceral fat area. Intriguingly, visceral fat area is an independent variable affecting arterial elasticity, but not IMT or PWV. Furthermore, multiple regression analysis revealed that arterial elasticity correlates strongly with visceral fat area.
Conclusions: Arterial elasticity value we measure is a new parameter for evaluating atherosclerosis in subjects with visceral adiposity and more sensitive than the currently established atherosclerosis values, carotid IMT and PWV. Measuring arterial elasticity has the potential to reveal minute vascular changes, and may have broad clinical applications for evaluating early stage atherosclerosis.

Obesity has increased dramatically, becoming a global epidemic in recent decades [1]. Obesity is closely associated with the development of atherosclerosis [2], via rising incidences of metabolic disorders, including diabetes, dyslipidemia, hypertension, inflammation, and the prothrombotic state [3]. Furthermore, obesity is involved in sympathetic nerve activation as well as cardiac structural and functional adaptations [4], and is reportedly an independent cardiovascular risk factor [5]. Recent studies have shown that adipocytokines, such as PAI-1, TNF-α and adiponectin, play crucial roles in the development of metabolic disorders and atherosclerosis, in various tissues including the vasculature [6]. In particular, visceral fat accumulation, rather than the body mass index (BMI) or subcutaneous fat accumulation, was shown to be strongly associated with various obesity-related disorders [7], and is thus considered to be a major risk factor for cardiovascular disease [8]. Many studies have shown that increasing body weight is closely related to the surrogate markers associated with atherosclerosis, such as carotid intima–media thickness (IMT) and pulse wave velocity (PWV). In addition, visceral adiposity is reportedly related to atherosclerosis, which is determined by carotid IMT [9–13], coronary calcification [14] and arterial stiffness [15,16]. In some reports, this relationship persisted after adjustments for multiple linear regression analysis [12–15]. While visceral fat areas were correctly measured by computed tomography (CT) scans in few studies [12,15], abdominal ultrasound was employed in many

* Corresponding author. Tel.: +81 22 717 7611; fax: +81 22 717 7611.
E-mail address: oka-y@mail.tains.tohoku.ac.jp (Y. Oka).

0021-9150/$ – see front matter © 2009 Elsevier Ireland Ltd. All rights reserved.
doi:10.1016/j.atherosclerosis.2009.01.046

reports [9–11,13,14,16], which is often imprecise to determine visceral fat area. It has been widely recognized that non-invasive methods of evaluating atherosclerosis have limitations, such as slow changes in carotid IMT and the influence of blood pressure on PWV. Thus, an accurate and practical means of evaluating atherosclerosis is needed.

Recently, we developed a novel non-invasive method for measuring a change in thickness of multiple layers preset in arterial wall during a single heartbeat [17,18]. Briefly, multiple points were preset from the luminal surface to the adventitia of the posterior wall along an ultrasonic beam and the displacements at these preset points were estimated by applying the phased tracking method to the received echo. A layer was defined as being between two points. A minute change in thickness of the layer was obtained by subtraction of the displacements at these two points and then, the strain of the layer was obtained by dividing the change in thickness by the original thickness set at the end diastole. By changing the depth and applying the same procedure, the strains at multiple depths in arterial wall were obtained at constant intervals, usually 80 μm. This innovative phased tracking method enables us to evaluate regional characteristics of the artery in detail; during a single heartbeat these sites either deform easily in soft regions or there is little deformation in hard regions. We integrated changes in thickness, which we describe with the term "arterial elasticity". This "arterial elasticity" measurement is a promising approach to evaluating atherosclerosis [19,20]. Therefore, we applied this method to in vivo detection of regional changes in human carotid arterial walls. In a study of subjects with type 2 diabetes, carotid arterial elasticity correlated significantly with currently established values for atherosclerosis, such as carotid artery IMT and PWV. Intriguingly, in subjects with IMT <1.1 mm, who are classified as not having atherosclerosis as defined by IMT criteria, arterial elasticity correlated with the number of risk factors, i.e. diabetes, dyslipidemia, hypertension and smoking, suggesting that arterial elasticity has potential for detecting early stage atherosclerosis. It was also suggested that measuring arterial elasticity would allow evaluation of qualitative changes in the carotid arterial wall [21].

Herein, to assess whether the effect of obesity on atherosclerosis can be evaluated using arterial elasticity, we examined the associations of obesity characteristics with atherosclerosis values including arterial elasticity, carotid IMT and PWV. We further evaluated the impact of fat distribution on atherosclerosis.

1. Methods

1.1. Study subjects

The study subjects were recruited from among patients with BMI over 30 at Tohoku University Hospital. Patients with type 1 diabetes, renal failure (serum creatinine >2.0 mg/dL), severe heart failure (NYHA functional class 2–4), atrial fibrillation and peripheral arterial disease were excluded from the study. The study protocol was approved by the Tohoku University Institutional Review Board. Informed consent was obtained from each patient.

We used the following criteria for the diagnosis of metabolic disorders. Diabetes was defined as fasting blood glucose ≥7.0 mmol/dl (126 mg/dl) and/or hemoglobin A1c ≥6.5%, based on the definition proposed by the Japan Diabetes Society, or taking antidiabetic drugs including insulin. Dyslipidemia was defined as LDL cholesterol ≥3.6 mmol/dl (140 mg/dl) and/or triglyceride ≥1.7 mmol/l (150 mg/dl), based on the definition proposed by the Japan Atherosclerosis Society in 2007, or taking lipid-lowering drugs. The subjects whose systolic blood pressure (BP) ≥140 mmHg and/or diastolic BP ≥90 mmHg (Japanese Society of Hypertension guidelines 2004) or who were taking antihypertensive drugs were defined as having hypertension. The subjects who currently smoked were classified as current smokers.

1.2. Measurement of arterial wall elasticity

Real-time measurement of regional elasticity in the far wall of common carotid artery (CCA) was achieved based on a previously described method [22] with ultrasound diagnostic equipment (prototype system by Panasonic), which was specialized for measuring regional elasticity. With this system, an ultrasound beam sequentially scanned an artery along its length at 32 positions at intervals of 200 μm with a linear type 7.5-MHz probe.

Multiple points were preset from the luminal surface to the adventitia along each beam at constant intervals of 80 μm, and the displacements at these preset points were estimated by applying the phased tracking method to the received echo. A layer was defined as being between two points, where the distance between these two points (i.e. the thickness of the layer) was set at 320 μm. As shown in Fig. 1C, minute changes in thickness of the layer were obtained by subtraction of the displacements at these two points and then, the strain of the layer was obtained by dividing the change in thickness by the original thickness (320 μm) which was set at the end diastole. By changing the depth of the layer at intervals of 80 μm and applying the same procedure, the strains at multiple depths were obtained at intervals of 80 μm.

The elasticity of each layer was obtained from the maximal strain and the pulse pressure measured at the upper arm. The maximal strain is defined by the absolute value of difference between the maximum and minimum of the measured change in thickness, as shown in Fig. 1C, and the maximal strain was determined at each location, independent of time.

Using the above procedure, the elasticity was obtained at intervals of 80 μm in the direction of depth and 200 μm along its length, as shown in Fig. 1B. Regional elasticity values of multiple sites in each layer were displayed as shown in Fig. 1A and a mean regional elasticity value (kPa) of bilateral CCA was used for analysis.

1.3. Measurement of carotid artery intima–media thickness

IMT of the carotid arteries was measured using ultrasound diagnostic equipment (EUB-450, Hitachi Medico, Tokyo, Japan) with an electrical linear transducer (center-frequency of 7.5 MHz). By B-mode ultrasound, CCA, carotid bulb, and portions of the internal and external carotid arteries on both sides were scanned with the subject in the supine position. IMT was measured at a point on the far wall of the CCA, 1 cm proximal to the bifurcation [23], from the longitudinal scan plane that showed the intima–media boundaries most clearly.

1.4. Measurement of PWV

PWV values were measured using an automatic waveform analyzer (BP-203RPE; Colin Co., Komaki, Japan) [24]. Pulse waves were recorded on the right brachial artery and both posterior tibial arteries. The average PWV was calculated by dividing the arm–ankle distance by the pulse wave transmission time between these points on both sides.

1.5. Measurement of abdominal fat area

Abdominal subcutaneous and intra-abdominal fat areas were measured by CT scans with a SOMATOM Definition (Siemens AG., Munich, Germany) at the level of the fourth lumbar vertebra. The border of the intra-abdominal cavity was outlined on the CT image and the total area of visceral fat was measured at an attenuation range of −200 and −50 Hounsfield units [25].

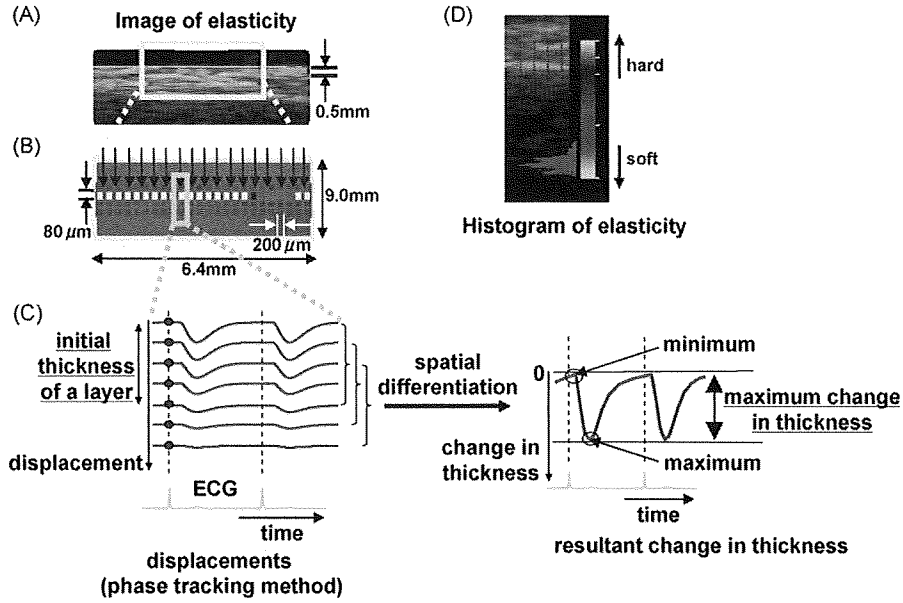

Fig. 1. Evaluation of carotid artery elasticity by phase tracking method. Arterial elasticity is displayed as a 2D cross-sectional color image, which is updated at every heartbeat (A). Multiple sites are preset from the luminal surface to the adventitia (113 depths × 32 beams per 9 mm × 6.4 mm scanned area) and elasticity in each module is measured by the phase tracking method (B). The arterial wall was divided into multiple layers with thicknesses set at 320 μm. The changes in thickness at each depth during the cardiac cycle are simultaneously obtained, and the maximum change in thickness corresponds to the elasticity in each module (C). The elasticity distribution is shown as a histogram (D).

1.6. Statistical analysis

Variables were compared using Pearson's regression analysis. Then, a multiple linear regression analysis was performed to evaluate the independent parameters that were significantly related to arterial elasticity. All data are expressed means ± S.D., and a p-value less than 0.05 was accepted as indicating statistical significance. All statistical analyses were performed using the Statistical Package for the Social Sciences version 13.0 (SPSS Japan Inc., Tokyo, Japan).

2. Results

The clinical characteristics of 78 subjects are shown in Table 1. Mean age is 41.0 ± 13.9 years, BMI 37.6 ± 7.2 (kg/m^2). Thus, the subjects were relatively young and categorized as having moderate, extreme or severe obesity according to Japanese guidelines.

To assess the clinical relevance of carotid artery elasticity in obese subjects, the arterial elasticity value was compared to atherosclerosis values obtained with currently established methods, carotid IMT and PWV. Arterial elasticity showed significant positive correlations with both carotid IMT (r = 0.422, p < 0.01) and PWV (r = 0.360, p < 0.01) in obese subjects (Fig. 2). Similar positive correlations among these three atherosclerosis values were observed in our previous results in subjects with type 2 diabetes [21]. The IMT value in this study was 0.61 ± 0.17 (range: 0.30–1.20) mm and PWV was 1396 ± 260 (range: 992–2117) cm/s, i.e. these obese subjects did not have advanced atherosclerosis, in contrast to the results in subjects with type 2 diabetes in our previous study (IMT: 0.94 ± 0.30 mm, PWV: 1703 ± 356 cm/s).

We then explored the association of carotid arterial elasticity with the clinical and demographic characteristics of these obese

Table 1
Subject characteristics.

Number	78
Age, years	41.0 ± 13.9
Gender (male), %	29.5
Body weight, kg	98.8 ± 24.2
BMI, kg/m^2	37.6 ± 7.2
Fasting blood glucose, mg/dl	121.3 ± 47.6
HbA1c, %	6.5 ± 1.8
Serum insulin μU/ml	17.8 ± 13.2
HOMA-R	4.5 ± 3.8
Systolic BP, mmHg	126.9 ± 14.4
Diastolic BP, mmHg	79.8 ± 10.7
Total cholesterol, mg/dl	208.2 ± 43.5
HDL cholesterol, mg/dl	45.8 ± 9.6
LDL cholesterol, mg/dl	132.6 ± 32.9
Triglyceride, mg/dl	184.1 ± 177.4
Uric acid, mg/dl	5.9 ± 1.5
Visceral fat area, cm^2	150.3 ± 55.7
Subcutaneous fat area, cm^2	405.7 ± 160.0
Diabetes, %	46.8
Dyslipidemia, %	60.3
Hypertension, %	48.7
Current smoker, %	28.0

Mean ± S.D.

Table 2
Associations between atherosclerosis values and subject characteristics.

Variables	r		
	Elasticity	IMT	PWV
Age	0.46**	0.44**	0.67**
Male	0.27*	0.24**	−0.086
Body weight	0.03	−0.075	−0.11
BMI	0.07	−0.06	0.045
Fasting blood glucose	0.14	0.032	0.14
HbA1c	−0.02	−0.036	0.0095
Total cholesterol	0.20	0.061	0.030
HDL cholesterol	−0.03	0.19	0.060
LDL cholesterol	0.15	0.034	−0.049
Triglyceride	−0.03	0.005	−0.040
Systolic BP	0.38**	0.27*	0.35**
Diastolic BP	0.28*	0.26*	0.047
Uric acid	0.15	0.10	−0.20
Diabetes	0.15	0.091	0.39**
Dyslipidemia	0.04	−0.11	0.037
Hypertension	0.37**	0.39**	0.51**

* p < 0.05.
** p < 0.01.